Strong Warming over the Antarctic Peninsula during Combined Atmospheric River and Foehn Events: Contribution of Shortwave Radiation and Turbulence

Xun Zou[1], Penny Marie Rowe[2], Irina Gorodetskaya[3], David H. Bromwich[4], Matthew Lazzara[5], Raul R. Cordero[6], Zhenhai Zhang[7], Brian Kawzenuk[8], Jason M. Cordeira[9], Jonathan D Wille[10], F. Martin Ralph[11], and Le-sheng Bai[12]

[1]University of California, San Diego
[2]NorthWest Research Associates
[3]University of Aveiro
[4]Ohio State University
[5]University of Wisconsin-Madison
[6]USACH
[7]UC San Diego
[8]Scripps Institution of Oceanography
[9]Plymouth State University
[10]Université Grenoble Alpes
[11]SIO
[12]Byrd Polar Research Center

October 6, 2023

JGR Atmospheres

RESEARCH ARTICLE
10.1029/2022JD038138

Strong Warming Over the Antarctic Peninsula During Combined Atmospheric River and Foehn Events: Contribution of Shortwave Radiation and Turbulence

Xun Zou[1], Penny M. Rowe[2], Irina Gorodetskaya[3,4], David H. Bromwich[5], Matthew A. Lazzara[6,7], Raul R. Cordero[8], Zhenhai Zhang[1], Brian Kawzenuk[1], Jason M. Cordeira[1], Jonathan D. Wille[9], F. Martin Ralph[1], and Le-Sheng Bai[5]

[1]CW3E, Scripps Institution of Oceanography, University of California San Diego, La Jolla, CA, USA, [2]North West Research Associates, Redmond, WA, USA, [3]Department of Physics, CESAM - Centre for Environmental and Marine Studies, University of Aveiro, Aveiro, Portugal, [4]CIIMAR | Interdisciplinary Centre of Marine and Environmental Research, University of Porto, Porto, Portugal, [5]Byrd Polar and Climate Research Center, The Ohio State University, Columbus, OH, USA, [6]Antarctic Meteorological Research and Data Center, Space Science and Engineering Center, University of Wisconsin-Madison, Madison, WI, USA, [7]Department of Physical Sciences, School of Engineering, Science, and Mathematics, Madison Area Technical College, Madison, WI, USA, [8]Department of Physics, University of Santiago de Chile, Santiago, Chile, [9]IGE/CNRS, University Grenoble-Alpes, Saint-Martin-d'Hères, France

Abstract The Antarctica Peninsula (AP) has experienced more frequent and intense surface melting recently, jeopardizing the stability of ice shelves and ultimately leading to ice loss. Among the key phenomena that can initiate surface melting are atmospheric rivers (ARs) and leeside foehn; the combined impact of ARs and foehn led to moderate surface warming over the AP in December 2018 and record-breaking surface melting in February 2022. Focusing on the more intense 2022 case, this study uses high-resolution Polar WRF simulations with advanced model configurations, Reference Elevation Model of Antarctica topography, and observed surface albedo to better understand the relationship between ARs and foehn and their impacts on surface warming. With an intense AR (AR3) intrusion during the 2022 event, weak low-level blocking and heavy orographic precipitation on the upwind side resulted in latent heat release, which led to a more deep-foehn like case. On the leeside, sensible heat flux associated with the foehn magnitude was the major driver during the night and the secondary contributor during the day due to a stationary orographic gravity wave. Downward shortwave radiation was enhanced via cloud clearance and dominated surface melting during the daytime, especially after the peak of the AR/foehn events. However, due to the complex terrain of the AP, ARs can complicate the foehn event by transporting extra moisture to the leeside via gap flows. During the peak of the 2022 foehn warming, cloud formation on the leeside hampered the downward shortwave radiation and slightly increased the downward longwave radiation.

Plain Language Summary On the Antarctic Peninsula (AP), when ice shelves break up, glaciers flow faster from the land into the sea, leading to ice loss and increasing sea level rise. Surface warming is projected to double by 2050 over Antarctica and may have led to ice shelf collapse. Two phenomena that enhance surface warming are atmospheric rivers, (long corridors of moisture in the atmosphere) and leeside foehn effects (cooler and moist air advection on the upwind side that becomes warmer and drier when descending on the leeside). Here we study two combined atmospheric river and foehn events that led to surface warming on the AP, occurring in December 2018 and February 2022. The main warming mechanism in the northeastern AP during the nighttime was transfer of heat from the air to the ice surface (sensible heat flux), while the main mechanism during the daytime was intense sunlight, which was able to reach the surface because of clear skies on the opposite (lee) side caused by foehn. However, complicating the picture, there are gaps in the AP mountain range that let the atmospheric river through, allowing clouds to form on the other side, which then blocked some of the sunlight.

Key Points:

- This study investigates the atmospheric river and foehn warming over the Antarctic Peninsula via observations and model simulations
- Atmospheric rivers led to stronger precipitation on the upwind side and favored the foehn-related sensible heat transfer on the leeside
- Under the combined atmospheric rivers and foehn, shortwave radiation contributed the most to the ice surface warming, followed by sensible heat flux

Supporting Information:

Supporting Information may be found in the online version of this article.

Correspondence to:

X. Zou and P. M. Rowe,
x4zou@ucsd.edu;
penny@nwra.com

Citation:

Zou, X., Rowe, P. M., Gorodetskaya, I., Bromwich, D. H., Lazzara, M. A., Cordero, R. R., et al. (2023). Strong warming over the Antarctic Peninsula during combined atmospheric River and foehn events: Contribution of shortwave radiation and turbulence. *Journal of Geophysical Research: Atmospheres*, *128*, e2022JD038138. https://doi.org/10.1029/2022JD038138

Received 7 NOV 2022
Accepted 23 JUL 2023

Author Contributions:

Conceptualization: Xun Zou, Penny M. Rowe, Irina Gorodetskaya, David H. Bromwich, Jonathan D. Wille
Data curation: Xun Zou, Penny M. Rowe, Irina Gorodetskaya, Matthew A. Lazzara, Raul R. Cordero, Brian Kawzenuk

1. Introduction

The Antarctica Peninsula (AP) is one of Earth's fastest warming regions and has been experiencing intense ice loss in the last 60 years, except for a recent cooling since the late 1990s. (Jones et al., 2019; Shepherd et al., 2018). Surface melting due to atmospheric warming is the major contributor to ice shelf break-up over the AP (e.g., van

Formal analysis: Xun Zou, Penny M. Rowe, Irina Gorodetskaya, David H. Bromwich, Matthew A. Lazzara, Zhenhai Zhang
Funding acquisition: Xun Zou, Penny M. Rowe, Irina Gorodetskaya, F. Martin Ralph
Investigation: Xun Zou, Penny M. Rowe, Irina Gorodetskaya, David H. Bromwich, Matthew A. Lazzara, Zhenhai Zhang, Brian Kawzenuk
Methodology: Xun Zou, Penny M. Rowe, Irina Gorodetskaya, David H. Bromwich, Zhenhai Zhang, Jonathan D. Wille
Project Administration: Xun Zou, Penny M. Rowe, Irina Gorodetskaya
Resources: Xun Zou, Penny M. Rowe, Irina Gorodetskaya, David H. Bromwich, Raul R. Cordero, Le-Sheng Bai
Software: Xun Zou, Penny M. Rowe, Irina Gorodetskaya, Le-Sheng Bai
Supervision: Penny M. Rowe, Irina Gorodetskaya, David H. Bromwich, F. Martin Ralph
Validation: Xun Zou, Penny M. Rowe, Irina Gorodetskaya, David H. Bromwich
Visualization: Xun Zou, Penny M. Rowe, Irina Gorodetskaya, Matthew A. Lazzara, Brian Kawzenuk
Writing – original draft: Xun Zou, Penny M. Rowe, Irina Gorodetskaya, David H. Bromwich, Matthew A. Lazzara
Writing – review & editing: Xun Zou, Penny M. Rowe, Irina Gorodetskaya, David H. Bromwich, Matthew A. Lazzara, Raul R. Cordero, Zhenhai Zhang, Jonathan D. Wille, F. Martin Ralph, Le-Sheng Bai

den Broeke, 2005). In response to rapidly warming air temperatures, such as heat waves, surface melt is projected to increase in upcoming decades regardless of the emission scenario (Feron et al., 2021). Several Antarctic ice shelves have an increasing probability of reaching the record meltwater production that the Larsen A and Larsen B ice shelves exhibited before their collapse (Feron et al., 2021).

The rate of ice loss over the AP has tripled since the 1990s with an acceleration of 16 Gt yr^{-1} per decade (Rignot et al., 2019; Shepherd et al., 2018). Also, surface melting is projected to double by 2050 over Antarctica, especially over the AP, which can decrease the surface albedo and lead to the ice surface lowering and thinning (Paolo et al., 2015; Siegert et al., 2019; Tuckett et al., 2019). Surface meltwater produced during the warming will not only jeopardize the stability of ice shelves via hydrofracturing, but also release latent heat if the melting water in the perennial snowpack refreezes, and then lead to additional melting (Holland et al., 2011). In the past three decades, the northern AP has lost the Larsen A Ice Shelf in 1995 and the Larsen B Ice Shelf in 2002 (Rignot et al., 2004; Rott et al., 1996). Without the buttressing effect provided by ice shelves, ice loss over Antarctica will accelerate and contribute to global sea level rise. From 2003 to 2019, the floating and grounded ice loss over the AP has contributed 1.7 mm to sea level rise and has the potential to increase the sea level by 0.5 m if all ice melts (Smith et al., 2020).

The collapse of ice shelves over the AP is the consequence of multiple factors, including rapid regional atmospheric warming and an extended melting period (Mulvaney et al., 2012; Scambos et al., 2000). During the austral summer, warming over the northeast AP is strongly associated with strengthening westerly winds due to the positive Southern Annular Mode (SAM) trend (Clem et al., 2016, 2022; Elvidge & Renfrew, 2016; Marshall et al., 2006). Stronger summer westerly winds have led to a higher frequency of air masses being advected eastward over the orographic barrier of the northern AP (Marshall et al., 2006), contributing to foehn-induced surface melt of ice shelves on the eastern side of the Peninsula (Bozkurt et al., 2018; González-Herrero et al., 2022). Also, associated with a warming tropical Atlantic sea surface temperatures, a deepened Amundsen Sea Low favors warm air advection and the surface warming over the AP (Li et al., 2021). Deep convection in the central tropical Pacific often leads to prolonged cyclone activity over the South Pacific and blocking highs/anticyclones over the Drake Passage, which helps transport warm marine air toward the southwest AP (Clem et al., 2022). This circulation pattern may be associated with strong atmospheric rivers (ARs) and foehn warming on the leeside of the AP due to orographic lifting on the upwind side (Clem et al., 2022). However, the surface warming/melting pattern depends on the strength and landfall location of an AR, as well as its modification by the local topography.

Previous ice shelf break-ups have been influenced by ARs and foehn (Wille et al., 2022). Polar ARs are moisture from lower latitudes that travel to the polar region via a long narrow corridor of water vapor transport (Gorodetskaya et al., 2020; Ralph et al., 2004; Terpstra et al., 2021; Wille et al., 2022). Foehn wind is a warm and dry descending air on the leeside of the mountain barrier, which results from relatively cooler and moist air advection on the upwind side (WMO in 1992). ARs can trigger foehn warming and lead to record-breaking temperatures, such as the warm event (max 2 m temperature of 17.5°C) observed at Esperanza station in March 2015 (Bozkurt et al., 2018; Xu et al., 2021). Foehn warming in the polar regions triggered by ARs has been observed over the AP (e.g., Bozkurt et al., 2018; Wille et al., 2019), West Antarctica (e.g., eastern Ross Ice Shelf, Zou et al., 2021a), and Greenland (Mattingly et al., 2020). Standalone foehn events (without AR impacts) may generally have a smaller warming extent across the Larsen ice shelves than those associated with intense ARs (Wille et al., 2022).

A variety of mechanisms contribute to foehn warming, including latent heat release on the upwind side from orographic precipitation, adiabatic warming from the descending air, sensible heat transfer from upper foehn flow to the ice surface via turbulence, and enhanced radiative heating due to foehn clearance; in turn, these contribute to surface warming/melting on the leeside (Elvidge & Renfrew, 2016). Larsen Ice Shelf is frequently under the impact of foehn warming, especially at the mountain base and the northern AP region (Turton et al., 2018). Extra moisture flux from ARs can amplify foehn warming due to increased latent heat release (Bozkurt et al., 2018). Thus, analysis of detailed mechanisms of surface warming under combined ARs and foehn can help us better understand the ice shelf stability and will benefit future projections of sea level rise.

Despite knowledge gains from previous studies, the detailed physical mechanism of surface melting on the AP under the combined impact of ARs and foehn is still unclear. First, with different circulation patterns, the water vapor flux or transport within the AR may or may not hit the mountain range over the AP perpendicularly, which significantly affects the formation of the foehn wind. Also, the northern tip of the AP projects eastward, which

indicates that the southern and northern AP might experience different magnitudes of warming under the same foehn event. Second, the strength of radiative heating depends both on cloudiness and on solar elevations which are low over the AP. Previous studies have found radiative heating on the AP is relatively small in a deep-foehn case during early summer (Elvidge & Renfrew, 2016); however, it is important to address whether this is always the case. Third, the topographic barrier over the AP has several gaps (or lower elevations), which can allow extra moisture from ARs to reach the leeside directly (e.g., foehn jets; Laffin et al., 2022). This can weaken the intensity of orographic precipitation on the upwind side and foster cloud formation from the extra moisture on the leeside, complicating the foehn-cloud clearance effect (Elvidge et al., 2020) by reducing the shortwave downward radiation (SWD), and thus the radiative heating. In addition, these foehn jets have contributed to surface melting due to enhanced sensible heat flux (SHF) transfer to the surface (Elvidge et al., 2015).

This work investigates two representative AR/foehn cases in 2018 and 2022 via high-resolution Polar Weather Research and Forecasting model (PWRF) simulations with advanced model configurations. These two cases demonstrate different types of AR and their contrasting impacts on the surface melting. During the 2018 event, the AP region experienced a moderate AR from a zonal direction. The AR in 2022 is stronger and from a meridional direction with a longer duration. The difference in the direction of integrated vapor transport (IVT) results in divergent modifications of the airflow by local topography, which is critical for foehn formation. Although ARs are linked to limited melt cases over the AP during austral summer, they significantly contribute to the widespread and intense foehn warming/melting on the eastern side (Wille et al., 2022). Also, intense ARs do occasionally generate surface melt outside of the summer months (Kuipers Munneke et al., 2018), the ARs chosen here represent the greatest surface melt consequences. Section 2 describes the data and PWRF model settings. Section 3 presents the evaluation of PWRF simulations by comparison to observations from weather stations and radiosondes, analyzes the regional circulation pattern, and investigates the contribution of AR/foehn to the leeside warming. Section 4 discusses the relationship between AR and foehn in the 2022 case, and their combined impact on the surface melting. A comparison of AR/foehn cases between the AP and West Antarctica (WA) is also presented. Section 5 summarizes the results from the previous analysis.

2. Data and Methods

2.1. ERA5 Reanalysis Data

This study uses the 5th major atmospheric reanalysis (ERA5) and the land data set (ERA5 Land) produced by the European Centre for Medium-Range Weather Forecasts (ECMWF; Hersbach et al., 2018; Muñoz Sabater, 2019). By combining model simulations with observations, ERA5 provides hourly output with 31 km horizontal resolution and 137 vertical levels. Compared to its predecessor, ERA-Interim, ERA5 significantly improved results in the troposphere with a shorter latency, including conservation of potential temperature (Hersbach et al., 2020; Hoffmann et al., 2019). Synoptic- and meso-scale features, such as cyclones, convective updrafts and gravity waves are better described in ERA5 (Hoffmann et al., 2019). Also, ERA5 outperforms other reanalysis products in describing stratospheric ozone depletion, which is critical for atmospheric changes in the high-latitude Southern hemisphere (Davis et al., 2017; Hersbach et al., 2020). Over the AP, ERA5 provides reliable information on surface temperature, wind speed, and humidity, especially at higher elevations (Tetzner et al., 2019). ERA5 Land with 9 km horizontal resolution is used to provide surface melting conditions for the case study. Driven by ERA5, ERA5 Land implements a correction in the thermodynamic near-surface state and reduces the error in skin temperature (Muñoz-Sabater et al., 2021).

2.2. Observations

PWRF surface simulations, including surface pressure, 2m temperature, and 10 m wind speed were compared to station observations (Escudero; upwind side) and observations from Automatic Weather Stations (AWS) or manual stations on the upwind side (Vernadsky and Rothera) and on the leeside (Esperanza, Marambio, and Larsen C) of the AP. Weather station data were obtained from the Antarctic Meteorological Research and Data Center (AMRDC; https://amrdcdata.ssec.wisc.edu/) at the University of Wisconsin-Madison (Lazzara et al., 2012), and from the OGIMET website (https://www.ogimet.com/). Three-hourly observations were used.

In addition, this study uses Antarctic composite infrared satellite imagery data for both 2018 and 2022 cases from the AMRDC. The Worldview tool from NASA's Earth Observing System Data and Information System

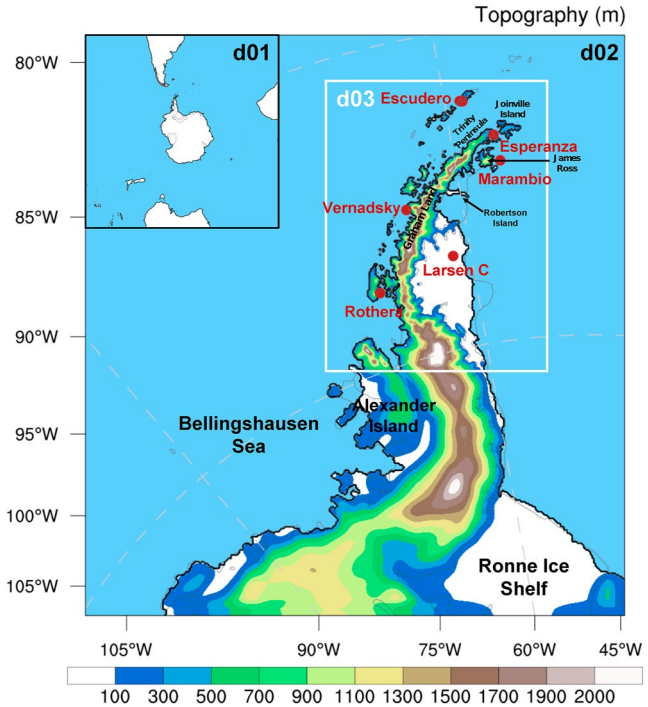

Figure 1. Map of the Antarctic Peninsula showing the PWRF domains (D01 30 km, D02 6 km, D03 1.2 km) and Reference Elevation Model of Antarctica (REMA) topography. Red dots indicate the locations of available surface stations.

(EOSDIS) provides additional satellite imagery on cloud conditions over the AP. Daily cloud conditions are observed from Moderate Resolution Imaging Spectroradiometer (MODIS) Corrected Reflectance (utilized from MODIS Level 1B data) on the Aqua and Terra satellites.

PWRF atmospheric profiles of temperature, humidity, and winds are compared to all available radiosonde measurements from three Antarctic stations: Escudero, Rothera and Marambio for the two case study periods. At Rothera, radiosondes were launched almost daily at 1200 UTC during 2018–2022. Unfortunately, only one radiosonde was launched at Rothera during the 2022 case study. At Marambio, radiosondes were launched less frequently, and only one radiosonde is available for each case study. By contrast, intensive extra observing activities were conducted at Escudero during the two case study time periods (including launching 7 radiosondes in 2018 and 5 radiosondes in 2022) as part of the Polar Prediction Project (PPP), a 10-year (2013–2022) initiative of the World Meteorological Organization's (WMO) World Weather Research Programme (WWRP) (Bromwich et al., 2020; Gorodetskaya et al., 2023).

The AP ice shelves experience persistent summer melt ponds, and surface melting and refreezing that reduce the surface albedo, leading to a positive snowmelt-albedo feedback and accelerating melting (Feron et al., 2021; Jakobs et al., 2021). Thus an accurate model surface description in PWRF is critical for the estimation of surface warming/melting (Luckman et al., 2014; Turton et al., 2018). Instead of the default albedo in WRF, we use observed daily surface albedo from MODIS as an initial field in model simulations (hereafter referred to as MODIS albedo; Schaaf & Wang, 2021; Wang et al., 2015; Figures S1a and S1b in Supporting Information S1). The MODIS albedo is produced by the National Aeronautics and Space Administration (NASA) based on 16 days of Terra and Aqua MODIS observational data. The MODIS albedo has been tested in the surface melting study over WA, where it was shown to lead improvements in the surface temperature estimation (Zou et al., 2021a). Also, the systematic cold bias over the Tibetan Plateau in WRF has been reduced by including the MODIS albedo. Created from stereophotogrammetry and satellite imagery, the Reference Elevation Model of Antarctica (REMA) provides a high-resolution surface elevation data set with a spatial resolution of up to 8 m (Howat et al., 2019). REMA surface elevation at 1 km resolution is introduced in PWRF simulations to better describe the modifications of the airflows by the local topography (Gerber & Lehning, 2020).

2.3. Polar WRF and Antarctic Mesoscale Prediction System (AMPS)

Developed and maintained by the Polar Meteorology Group of the Byrd Polar and Climate Research Center at The Ohio State University (Bromwich et al., 2013; Hines & Bromwich, 2008; Hines et al., 2019; Listowski & Lachlan-Cope, 2017; Xue et al., 2022), PWRF is a regional numerical prediction model based on WRF. This study used PWRF V4.3.3 to produce hourly output with a downscaling method, which includes three domains: domain 1, at 30-km resolution; domain 2, at 6-km resolution, and domain 3, at 1.2 km resolution (Figure 1). Except where noted, results and figures use the high-resolution domain 3 output, which covers the AP region. All PWRF outputs used in this paper are initialized at 0000 UTC, discarding the first 24 hr as spin-up time.

Table 1 shows the input data and physical parameterization settings in PWRF. Supercooled liquid water in clouds is always challenging to predict in the numerical weather models over the Southern Ocean (e.g., Bodas-Salcedo et al., 2016; Listowski et al., 2019). More advanced microphysics schemes provide more realistic cloud liquid water simulations, which is critical for estimation of the surface energy balance (Hines et al., 2019; Listowski et al., 2019). Instead of using an arbitrary categorization of frozen hydrometers, the two-moment Morrison-Milbrandt P3 (P3) adopts a continuum of particle properties for clouds (Hines et al., 2019, 2021). P3 provides the best estimation of liquid water path and longwave radiation from clouds compared to two other advanced schemes, Morrison two moment and Thompson (Hines et al., 2019). Thus, P3 is selected for the microphysics scheme, and the Mellor–Yamada–Nakanishi–Niino (MYNN; Nakanishi & Niino, 2006) is used for the

Table 1
PWRF Model Settings

	PWRF V4.3.3
Input data	ECMWF reanalysis data (ERA5)
Horizontal resolution	30 km/6 km/1.2 km
Vertical levels	71 levels (lowest level 4m above the surface)
Temporal resolution	Hourly
Spin-up	24 hr
Microphysics	P3
PBL scheme	MYNN
Shortwave and longwave	Both RRTMG
Land surface options	Noah MP
Surface layer options	MYNN
Surface albedo	MODIS (MODIS/Terra + Aqua BRDF/Albedo Daily L3 Global 0.05 Deg; black-sky albedo)
High-resolution topography	REMA 1 km topography
Nudging	Every 6 hr; nudging to u, v wind, temperature, and water vapor from ERA5 for model level 40 (~400 hPa) and above

atmospheric boundary layer scheme. Both longwave and shortwave radiation use the Rapid Radiative Transfer Model (RRTMG; Clough et al., 2005) or Global Climate/Circulation Models. We also use the Kain–Fritsch scheme for cumulus parameterization (only for domain 1) and Noah-MP for the land surface model (Kain, 2004; Niu et al., 2011). Most importantly, REMA 1 km topography information and MODIS observed surface albedo, described previously, are included in the input data to provide a better surface description (Howat et al., 2019; Corbea-Pérez et al., 2021; Figure S1 in Supporting Information S1). To avoid model instabilities, topographic smoothing has been applied to PWRF simulations. Adopting several PWRF settings, the Antarctic Mesoscale Prediction System (AMPS) outputs are used in this paper to provide default albedo and landmass in PWRF. AMPS, developed by the National Center for Atmospheric Research (NCAR), provides high-resolution weather forecasts to support the operations of the US Antarctic Program (Powers et al., 2012).

2.4. Polar Atmospheric River Scale

Compared to the mid- and low-latitudes, Antarctica has a colder, drier, and more pristine environment. Thus, the Center for Western Weather and Water Extremes (CW3E) group at Scripps Institution of Oceanography developed an AR scale specific to the polar regions, the Polar AR scale (eight rankings from AR A1 to AR5; Figure S2 in Supporting Information S1), to rank ARs over the AP at a given geographic location (Figure S2 in Supporting Information S1). The Polar AR scale was widely tested during the Year of Polar Prediction in the Southern Hemisphere (YOPP-SH) Winter Targeted Observing Periods, and has been proven to reflect the strength and duration of ARs accurately, which benefits both forecast operations and research (Bromwich et al., 2020; Ralph et al., 2019).

After using PWRF domain 3 outputs to identify AR intrusions, the hourly IVT is calculated as follows:

$$\mathrm{IVT} = \sqrt{\left(\frac{1}{g}\int_{1000}^{10} qu\mathrm{d}p\right)^2 + \left(\frac{1}{g}\int_{1000}^{10} qv\mathrm{d}p\right)^2} \quad (1)$$

where g is the gravity acceleration constant (m s^{-2}), q is specific humidity (kg kg^{-1}), u and v are zonal and meridional wind (m s^{-1}), and dp is the differential pressure (hPa).

3. Results

3.1. Evaluation of PWRF Results

PWRF simulation outputs were compared to station and AWS 3-hourly observations and ERA5 reanalysis data. Overall, PWRF was found to reliably simulate the synoptic circulation pattern (not shown) and surface conditions

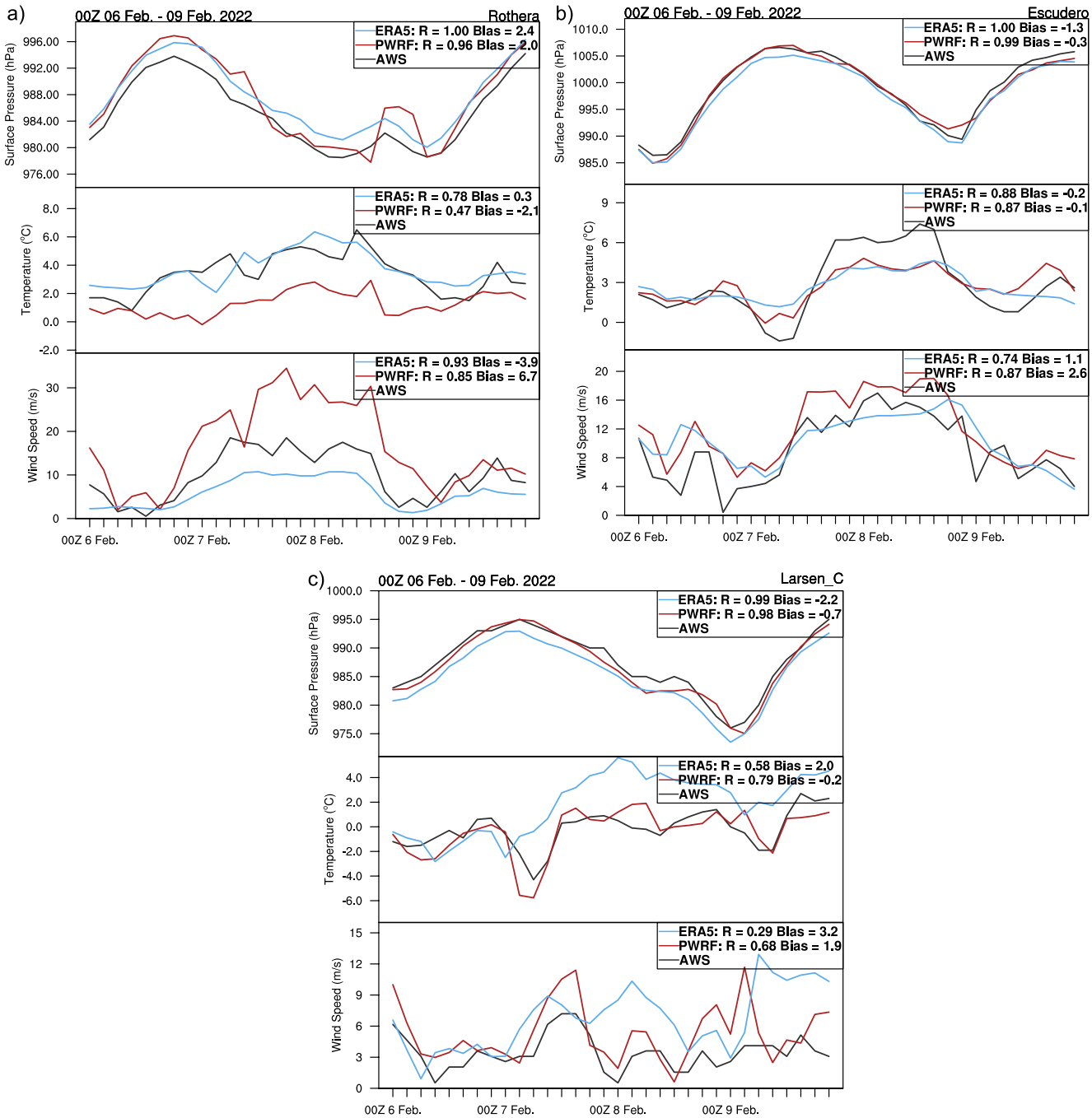

Figure 2. Evaluation of PWRF D03 (1.2 km) simulations and ERA5 reanalysis data (re-grid to PWRF D03) of surface pressure (top panels in a–c), 2 m temperature (middle panels), and 10 m wind speed (bottom panels) through comparison to automatic weather station (AWS) measurements at Rothera (a), Escudero (b), and Larsen C (c) every 3 hr. The correlation coefficient (R) and bias between PWRF simulations/ERA5 reanalysis data and station observations are shown at the top right corner of each panel.

compared to ERA5. Figure 2 shows the comparison of three basic surface variables between weather station observations and PWRF domain 3 outputs/ERA5 reanalysis data at Rothera (upwind) and Larsen C (leeside) during the 2022 case. PWRF simulations have a weak negative bias (−0.2°C) in temperature and a moderate positive bias in wind speed (1.9 m/s) at the Larsen C Ice shelf, which reduces the bias in ERA5 reanalysis data due to higher horizontal resolution. At Rothera, where the topography is complex, PWRF has a larger bias in all variables, especially for the 10m wind speed during the peak of the foehn warming. In contrast, ERA5 reanalysis data

Table 2
PWRF/ERA5 Correlation Coefficient (R) and Bias at Several Weather Stations Based 3 hr Data From 0000 UTC 6 February to 2100 UTC 9 February 2022

	Surface pressure (hPa)				Temperature (°C)				Wind speed (m/s)			
	R		Bias		R		Bias		R		Bias	
Stations	P	E	P	E	P	E	P	E	P	E	P	E
Rothera	0.96	1	2.0	2.4	0.47	0.78	−2.1	0.3	0.85	0.93	6.7	−3.9
Vernadsky	0.96	0.99	−0.3	−0.3	0.78	0.76	0	−0.1	0.54	0.60	9.2	2.6
Escudero	0.99	1	−0.3	−1.3	0.87	0.88	−0.1	−0.2	0.87	0.74	2.6	2.6
Marambio	0.99	1	2.2	0.6	0.53	0.52	−3.3	−1.9	0.74	0.83	1.2	−1.5
Larsen C	0.96	0.99	−0.7	−2.2	0.79	0.58	−0.2	2.0	0.68	0.29	1.9	3.2
Esperanza	0.94	0.94	2.0	0.5	0.27	0.69	−1.6	1.0	0.25	0.5	4.7	1.6
Average	**0.97**	**0.99**	**0.82**	**−0.05**	**0.62**	**0.70**	**−1.22**	**0.18**	**0.66**	**0.65**	**4.38**	**0.77**

Note. Gray shadow indicates stations located on the upwind side. P stands for PWRF and E stands for ERA5.

underestimates the wind speed. The 1.2 km horizontal resolution might be insufficient to capture the complex terrain on the upwind side and might introduce instabilities in model simulations. Thus, PWRF performs better in general at stations with a smoother surface. In addition, the average bias of 2 m relative humidity is 5% at Marambio and 1.3% at Escudero. On average, PWRF biases (Table 2) were found to be 0.82 hPa in surface pressure, −1.2°C in 2 m temperature, and 4.4 m/s in 10 m wind speed (2.6 m/s on the leeside and 6.2 m/s on the upwind side) at the selected AWS stations. In addition, compared with ERA5, PWRF simulations show a stronger barrier jet on the upwind side; further investigation into this result is needed.

Temperatures, relative humidities, and wind speeds in the troposphere from PWRF and ERA5 were compared to available station radiosonde measurements (Figures S3a and S3b in Supporting Information S1). Absolute maximum, mean, and root-mean-square (RMS) differences for temperature and wind speed are summarized in Table 3 for 2022. In 2022, the RMS difference in tropospheric temperature for PWRF simulations was 1.1°C (absolute maximum of 3.3°C and mean bias of −0.2°C), and the RMS difference in tropospheric wind speed was 3.7 m/s (absolute maximum of 10 m/s and mean bias of 0.9 m/s). Differences in 2018 (Table S1 in Supporting Information S1) were similar. Differences in relative humidity (RH) are complicated by high variability and occasional low biases in the radiosonde RH measurements, which are given in Tables S2 and S3 in Supporting Information S1. PWRF simulations show the

Table 3
PWRF Maximum (Max; Absolute) Differences, Mean Biases (Mean) and Root Mean Square Differences (RMS) in Tropospheric Temperature and Wind Speed, Compared to Radiosonde Data, at Several Stations During the 2022 Case Study

			Temperature (°C)			Wind speed (m/s)		
Stations	Date	Time	Max	Mean	RMS	Max	Mean	RMS
Escudero	2022/2/7	0	2.6	−0.1	0.7	6.7	0.9	2.0
	2022/2/7	12	2.1	−0.1	0.6	9.5	0.6	4.3
	2022/2/8	0	3.5	−0.3	1.2	20.0	2.5	5.1
	2022/2/8	23	4.2	0.2	1.5	7.4	−0.9	2.9
	2022/2/9	12	2.0	−0.2	0.9	8.0	0.8	3.3
Rothera	2022/2/9	12	5.8	−0.2	1.6	8.4	1.3	4.5
Marambio	2022/2/7	12	5.5	−0.5	1.6	10.6	0.6	3.9
Average			3.7	−0.2	1.1	9.9	0.8	3.7

Note. Gray shadow indicates stations located on the upwind side. The maximum, mean, and RMS differences are computed from the differences between radiosonde and PWRF temperatures/wind speeds within the troposphere. PWRF temperatures/wind speeds, which were originally at 27 pressure levels, from 1,000 to 100 hPa by 25 hPa, were first interpolated onto the same levels as the radiosonde, after which levels were restricted to the tropopause and the differences were computed.

Table 4
ERA5 Maximum (Max; Absolute) Differences, Mean Biases (Mean) and Root Mean Square Differences (RMS) in Tropospheric Temperature and Wind Speed, Compared to Radiosonde Data, at Several Stations During the 2022 Case Study

			Temperature (°C)			Wind speed (m/s)		
Stations	Date	Time	Max	Mean	RMS	Max	Mean	RMS
Escudero	2022/2/7	0	3.2	0.1	0.8	5.8	0.0	2.3
	2022/2/7	12	1.4	0.0	0.6	9.2	0.3	3.7
	2022/2/8	0	2.7	−0.3	1.0	16.2	1.3	3.9
	2022/2/8	23	5.7	0.7	1.6	6.6	−0.3	2.6
	2022/2/9	12	1.9	0.0	0.8	6.0	0.4	2.5
Rothera	2022/2/9	12	3.6	−0.1	1.1	11.5	−1.8	4.0
Marambio	2022/2/7	12	3.0	−0.3	1.2	8.8	0.7	3.5
Average			**3.1**	**0.0**	**1.0**	**9.1**	**0.1**	**3.2**

Note. Gray shadow indicates stations located on the upwind side. The maximum, mean, and RMS differences are computed from the differences between radiosonde and ERA5 temperatures/wind speeds within the troposphere. ERA5 temperatures and wind speeds were first interpolated onto the same levels as the radiosonde, after which levels were restricted to the tropopause and the differences were computed.

best agreement with station observations and ERA5 reanalysis for temperature, followed by wind speed (Table 4, and Table S4–S6 in Supporting Information S1). The overall good performance discussed above provides high confidence for us to use the PWRF simulation to analyze the two surface warming events over the AP.

3.2. December 2018 and February 2022 Surface Melt Events Over the Antarctic Peninsula

Two surface melting events that were triggered by the combined impact of ARs and foehn warming are studied, occurring on the northern AP in December 2018 and February 2022. In December 2018, a high precipitation amount (up to 5.7 mm/day) was observed at Vernadsky (Chyhareva et al., 2021), and surface melting also detected on the leeside based on National Snow and Ice Data Center (NSIDC) daily surface melt extent (not shown). At the beginning of January 2022, a large expanse of sea ice (about 2,000 km^2), which had persisted in the Larsen B embayment since 2011 and that can bond to and stabilize the ice shelves, began to break up between 17 and 19 January 2022 (acquired by MODIS on NASA's Terra and Aqua satellites). In the following February, under a La Niña condition and positive SAM (SAM index 1.92; Marshall, 2003), an unprecedented warming caused major surface melt over both western and eastern AP (Gorodetskaya et al., 2023). On 7–8 February 2022, several Antarctic stations observed record high temperatures, such as +12.7°C at Vernadsky, +13.6°C at Carlini, and +13.7°C at King Sejong (Gorodetskaya et al., 2023). The air temperature at Escudero remained above +6°C from 1800 UTC 7 February until 1500 UTC on 8 February.

3.3. Regional Circulation and Atmospheric River

The regional circulation significantly affects the strength and direction of ARs, and local topography impacts the orographic precipitation. Figure 3 shows 500 hPa geopotential height, horizontal wind from PWRF and the surface melting map from ERA5 Land for both 2018 and 2022 cases (e.g., 0000 UTC 6 December and 0000 UTC 8 February). Although both cases featured the development and propagation of two low-pressure centers, location of the lows varied, as well as the circulation pattern. In the 2018 case, the first low-pressure center developed over Pine Island Glacier at ~0000 UTC on 6 December (Figure 3a), and the secondary low developed over the Weddell Sea at ~0300 UTC on 7 December (not shown). These two lows covered the entire AP region, which led to zonal marine air advection over the northern tip of the AP for ~24 hr. In the 2022 case, the first low was located at coastal Pine Island Glacier (Figure 3b) and the second low migrated from the Bellingshausen Sea toward Alexander Island (not shown). Unlike the 2018 case, the 2022 case had a blocking high over the Weddell Sea (blue dashed line, Figure 3b). This low-high coupled pattern not only led to a stronger pressure gradient and marine air intrusion but also resulted in a stationary northerly flow lasting for 3 days, which transported extra moisture and heat from lower latitudes to Antarctica (e.g., Hirasawa et al., 2013). Using two polar-specific AR detection algorithms (see

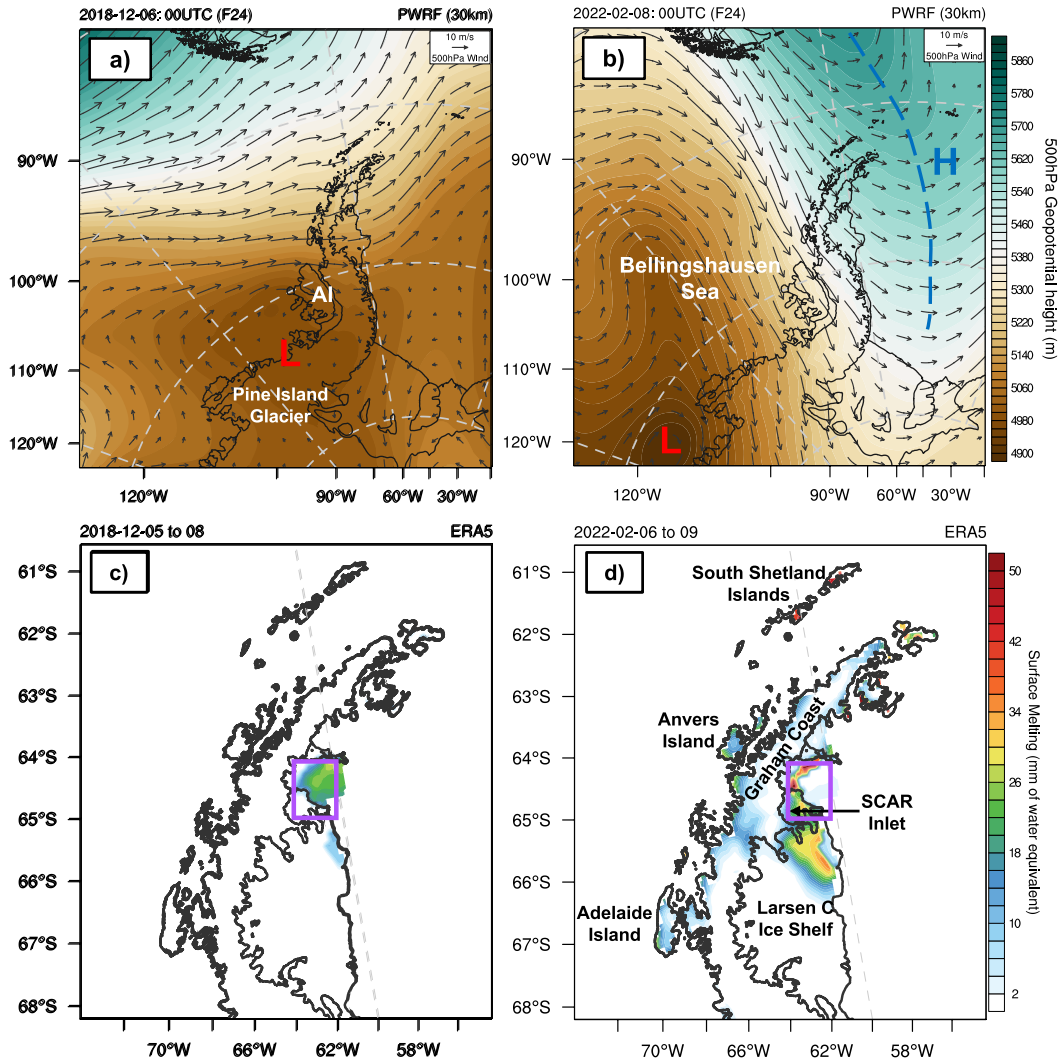

Figure 3. Circulation pattern and surface melting for the 2018 and 2022 cases. (a and b) show the 500 hPa geopotential height (contour fill) and wind field (black arrows) from PWRF D01 (30 km) at 0000 UTC 06 December 2018 and 8 February 2022. The blue "H" and dashed blue line represent the blocking high, and the red "L" represents the low-pressure center. (c and d) show the 3-day accumulated surface melting of water equivalent based on hourly ERA5 Land reanalysis data (9 km). AI: Alexander Island. The purple boxes in (c and d) indicate the AR/foehn "hotspot", which covers the SCAR inlet.

Wille et al., 2021), an AR was briefly detected northwest of the AP for the 2018 case, while in 2022, a prolonged AR was detected over the AP from 7 to 9 February following a shorter AR landfall on 5 February.

Compared to the 2018 case, the melting in the 2022 case impacts a broader area. In the 2018 case, the surface melting was mainly over the remaining Larsen B Ice Shelf (max ~30 mm of water equivalent; see Figure 3c). By contrast, in the 2022 case, surface melting affected the whole northern AP (Figure 3d), including the upwind side (e.g., Anvers Island, Graham Coast, and Adelaide Island; see also Gorodetskaya et al., 2023). The South Shetland Islands also experienced strong melting, whereas no melting was detected there in the 2018 case. On the leeside of the AP in the 2022 case, the intense melting (max >50 mm of water equivalent) covered the remaining Larsen B embayment, SCAR inlet, and the northern edge of the Larsen C Ice shelf, which are the focus areas of this research. The warming event in early February 2022 may have also contributed to the significant negative anomalies in sea ice extent observed in austral summer 2021-2022. In late February 2022, sea-ice extent hit its annual minimum at 1.9 million km^2, the absolute record low Antarctic sea-ice extent since the beginning of continuous satellite monitoring in 1979 (Wang, Luo, et al., 2022). Sea-ice extent remained close to record low levels during most of the summer 2021-22. It is worth mentioning that Antarctic sea ice has experienced an unexpected and

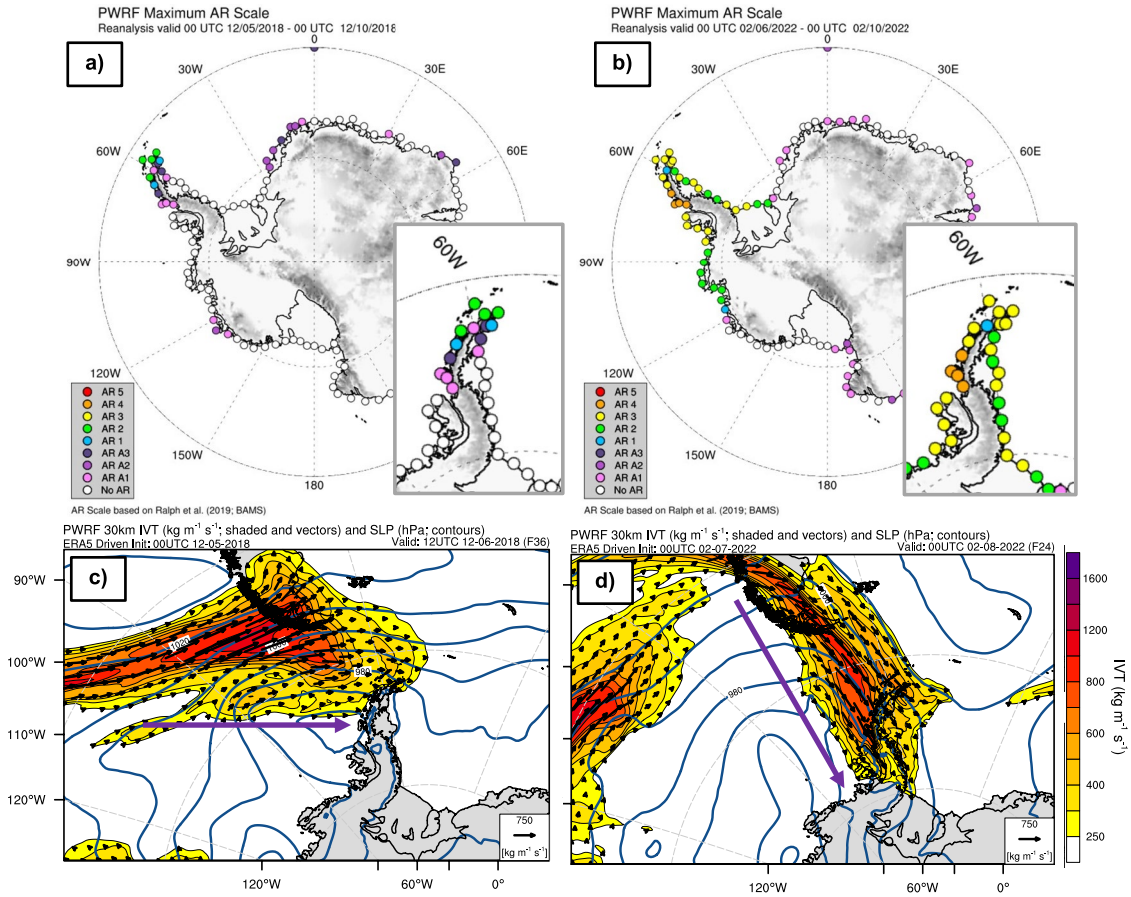

Figure 4. Strength of two Atmospheric River (AR) cases over the Antarctic Peninsula (AP) in (a) December 2018, and (b) February 2022, shown as the magnitude of the Polar AR scale along the coast (colored circles). The Polar AR scale magnitude is estimated using the integrated vapor transport (IVT) duration and magnitude simulated in PWRF domain 1 simulations at each grid location along the coast (see text). The IVT is shown in panels (c) and (d) for December 2018 and February 2022, respectively. Navy lines in (c and d) represent the mean sea level pressure (interval: 10 hPa) and purple arrows represent the direction of the AR intrusion.

significant reduction since 2016 with the equivalent of the 30-year sea ice loss in the Arctic between 2019 and 2021 (Eayrs et al., 2021).

Using PWRF simulations, the maximum AR scale was found to be a moderate AR2 (Figure 4a), according to the Polar AR scale (Figure S2 in Supporting Information S1). Consistent with the regional circulation, in 2018 the AR only affected the northern tip of the AP, as indicated by the IVT (Figure 4c). During the 2022 event, the entire AP region and the Filchner–Ronne Ice Shelf were all under the strong impact of AR3 with a max AR4 over Adelaide Island (Figures 4b and 4d; Table 5). ERA5 generally agrees with PWRF on the AR scale, except for a few spots adjacent to Adelaide Island where ERA5 indicates AR3 (not shown). The IVT pattern clearly shows the difference between these two cases. With a more zonal wind during the 2018 event (Figure S4a in Supporting Information S1 gray arrow, e.g., 0600 UTC 6 December 2018), southern Graham Land experienced nearly perpendicular moist air advection (Figure S4a in Supporting Information S1 solid brown box). Under this circumstance, the Larsen C Ice Shelf was most likely under foehn warming. Over the Trinity Peninsula, where the topographic barrier tilts eastward, the marine air intrusion approached the coast at a ~45° angle (Figure S4a in Supporting Information S1 blue dashed box). Thus, the foehn warming was weaker over the original Larsen A and B Ice Shelves (hereafter referred to as Larsen A and Larsen B). However, in the 2018 case, upcoming wind is not strong enough to trigger widespread foehn warming over the Larsen C Ice shelf, and Larsen A and B experienced moderate surface warming. By contrast, the 2022 case had a perpendicular airflow over the Trinity Peninsula due to a northerly wind pattern (Figure S4b in Supporting Information S1, gray arrow, e.g., 0000 UTC 8 February 2022), and the northern AP was under a stronger foehn warming (Figure S4b in Supporting Information S1 solid blue box). The direction, strength, and duration of the noted ARs are important because they affect the magnitude of the foehn warming on the leeside.

Table 5
Overview of 2018 and 2022 Cases

	2018	2022
Maximum AR detected	AR2 (ERA5)	AR3 (ERA5) and AR4 (PWRF)
AR duration	1 day	3 days
AR impact area	Upwind side of the northern tip of the AP	Entire AP region, coastal Pine Island Glacier and Ronne Ice Shelf.
AR direction	AR hits the AP via southwesterly wind	AR hits the AP via northwesterly wind
AR peak	2018-12-06 ~06UTC	2022-02-07 ~00UTC @Palmer land region2022-02-07 ~12UTC @upwind side of the AP
Foehn peak	2018-12-06 ~12UTC	00UTC 02-08-2022–00UTC 02–09 2022
Max. temp on the leeside	11 °C	18 °C

3.4. Foehn Warming and AR Impacts

Both the 2018 and 2022 case experience foehn warming on the leeside, however this study focuses on the 2022 event due to its broader impact (Figures 3c and 3d and 4). For the 2018 case, the surface warming mainly occurs along the mountain base and then expands to the Larsen ice shelves, which only last for ~24 hr. Over the Larsen B region (indicated previously with a purple box in Figure 3d), the average 2 m temperature increased ~3°C within 12 hr (from 0000 UTC 6 to 1200 UTC 6 December 2018) and above freezing point 2 m temperature lasted for ~10 hr (Figure S5a in Supporting Information S1). The skin temperature (over land only) confirms a moderate surface melting that lasted ~6 hr during the foehn period. On the leeside of the AP, there are two warming spots during the 2022 foehn case. One is over the Larsen B embayment (including the SCAR Inlet) and the other is adjacent to James Ross Island (Figure 5). The Larsen C Ice shelf did not experience widespread warming, except for the northern edge. Over the Larsen B region (purple box in Figure 3d), the average 2 m temperature increased more than 5°C and the average 10 m wind speed increased ~8 m s^{-1} within 24 hr (from 0000 UTC 7 to 0000 UTC 8 February 2022, second foehn period; Figure S5b in Supporting Information S1). The average 2 m relative humidity dropped by 20% after the peak of AR/foehn impact (Figure S5b in Supporting Information S1). The 2 m temperature above freezing point lasted for ~30 hr during the second foehn period, which was 3 times longer than the 2018 case. The skin temperature over ice shelves reached 0°C for 29 hr and remained high even after the foehn warming. The barrier jets on the upwind side indicate weak low-level blocking (e.g., Figures 5f and 5h). While both ERA5 and PWRF captured the two warming hotspots (Figure 5), the 2 m temperature in ERA5 was sometimes 4°C warmer than PWRF over Larsen B, especially at the beginning of this warming event (e.g., compare panels a and b in Figure 5). Larsen B is a mixture of open water and floating ice during the 2022 case. ERA5 indicates this area as land/ice shelves based on its land-sea mask variable, and PWRF has updated this area as open water via REMA data set. Further analysis is needed to explain this difference.

The cross-section of temperature and wind speed confirms the strong foehn warming (Figure 6 and Figures S7b and S7d in Supporting Information S1). Temperature inversions were observed on the upwind side, with a warm core ~700 m above the surface, and intense mountain waves were captured on the leeside (e.g., Figure 6g). Such temperature inversions reflect a more-stratified atmosphere in the 2022 case, which could enhance low-level blocking on the upwind side, and adiabatic warming on the leeside (Elvidge et al., 2015). However, the strong incoming wind brought by ARs can force the low-level air to pass over the mountain peak (compensate for the low-level blocking) and enhance the latent heat release on the upwind side. Furthermore, the strong mountain waves on the leeside transfer sensible heat from the upper warm foehn flow to the leeside surface of SCAR Inlet. The short-lived 2018 case, by contrast, has much weaker mountain waves and more moderate foehn warming on the leeside (Figures S5a, S6, and S7 in Supporting Information S1). The foehn warming mainly affects the leeside of the James Ross Island and the mountain base in the northern AP.

The two major drivers of surface melting over SCAR Inlet were found to be strong SWD during reduced cloudiness due to foehn clearance and SHF transferred to the surface by the mountain waves. However, the main driver of surface melting was found to differ between daytime and nighttime. During the day, net shortwave radiation (SW_{net}) is the leading contributor, ranging from 400 to 700 Wm^{-2} (for all time steps; not shown). Sensible heat flux, as the secondary factor during the daytime, can reach up to 300 Wm^{-2} (for all time steps; not shown). During the night, SHF maintains its strength, while the net shortwave radiation drops to 0 Wm^{-2} (not shown). The SHF is strongly correlated with the magnitude of the foehn, while the SW_{net} is considerably more complicated. Also, the SHF exhibits a wave pattern for multiple time steps during the 2022 event, especially closer to the mountain base. The variability in temperature and vertical wind speed within stationary orographic gravity waves (e.g., Figure S7 in Supporting Information S1) results in the stripe pattern in, SHF, 2 m temperature and 10m wind speed (blue oval; Figures 7 and 8). This pattern is consistent with mountain waves captured in the cross-section (Figure 6) and cloud conditions from the Antarctic infrared composite (Figure 7a) and MODIS corrected reflectance image (Figures S8c and S8d in Supporting Information S1).

During the 2022 case, weak low-level blocking and intense precipitation on the upwind side can lead to clear sky and stronger foehn warming on the leeside (e.g., Figure 7a, and Figure S8d in Supporting Information S1). However, there is a gap between Trinity Peninsula and Joinville Island, which allows moist

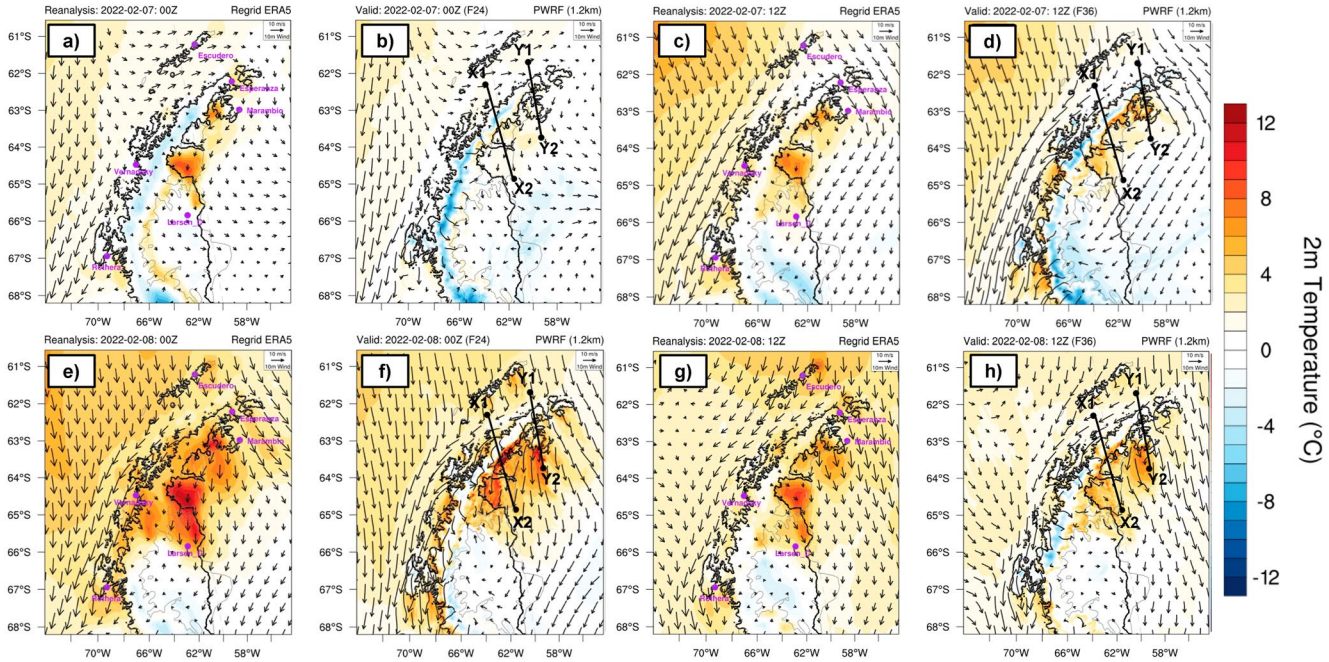

Figure 5. 2 m temperature and 10 m wind field over the Antarctic Peninsula from ERA5 reanalysis data and PWRF simulations at 0000 UTC 07 February 2022 (a and b); 1200 UTC 07 February 2022 (c), (d); 0000 UTC 08 February 2022 (e and f); and 1200 UTC 08 February 2022 (g and h). Solid black lines represent the two cross-sections shown in Figure 6. Purple dots represent the locations of observations. Coastline information is from the REMA topography data set. The ERA5 land-sea mask contains the fraction of land within every grid box. Over Antarctica, it is defined by the RAMP-2 data set, which does not include the 2002 Larsen B Ice Shelf collapse.

marine air to reach the leeside and form clouds, especially low- and mid-level liquid clouds (e.g., Figure 7a and Figure S9a in Supporting Information S1). The foehn jets going through the lower elevation in Graham Land can also transport extra moisture. When foehn warming is powered by the AR, the moisture transport can be strong through those gaps. Thus, the foehn clearance can be compensated for by clouds formed from the moisture in the gap flows; given that cloud conditions can vary significantly with time (Figure S8 in Supporting Information S1), the resulting SWD can be highly varying. Similar enhanced cloud impacts on the leeside were observed for the 2018 case. Taking SCAR Inlet as an example, the SW_{net} (average 69 Wm^{-2}) contributes ~1.3 times as much as the SHF (average 54 Wm^{-2}) to the surface melting/warming from 0000 UTC 6 February to 2300 UTC 9 February (Figure 9). The maximum of the SHF occurs at 0300 UTC on 8 February, which is around the foehn peak (Figure 9c). Orographic lee waves on the leeside transfer the sensible heat from upper foehn flow to the surface. The LHF contributes to the surface melting over the SCAR Inlet during the peak of foehn warming (8 February) with a maximum value > 60 Wm^{-2}. However, the warming from LHF is inconsistent during the event, which results in a weaker overall contribution compared to SWD and SHF. Trajectory analysis is needed to better explain the impact of LHF. Compared to PWRF simulations, ERA5 exhibits a similar pattern of SWD (Figure S10a in Supporting Information S1), albeit with a weaker foehn clearance on the leeside on 9 February. The impact of SHF in ERA5 is only half of that simulated in the PWRF (Figures S9b, S9c, and S10b in Supporting Information S1). Due to its coarser horizontal resolution, ERA5 is not specifically designed to capture small-scale features like mountain waves. Consequently, this limitation could result in cloud misrepresentation and an underestimation of turbulence on the leeside (Figure 9c). These findings are further supported by the inconsistent results in temperature and wind speed between ERA5 and the AWS station at Larsen C North (Figure 2). Additionally, Laffin et al. (2021) proposed that ERA5 underestimated the wind speed on the leeside of the AP during a foehn event in late May 2016.

Overall, SW_{net} is the major contributor to the surface warming over most of the ice surface on the leeside, except the mountain base or areas strongly affected by the cloud formation, where the SHF has an equal impact as SW_{net} (both ~140 Wm^{-2}; Figure 9). The dominant contribution of SW_{net} after the foehn event mainly comes from stronger SWD with time due to clear sky conditions (Figure S8e in Supporting Information S1). The combined AR/Foehn event can be more complicated due to the extra moisture input via dampened foehn effect over lower

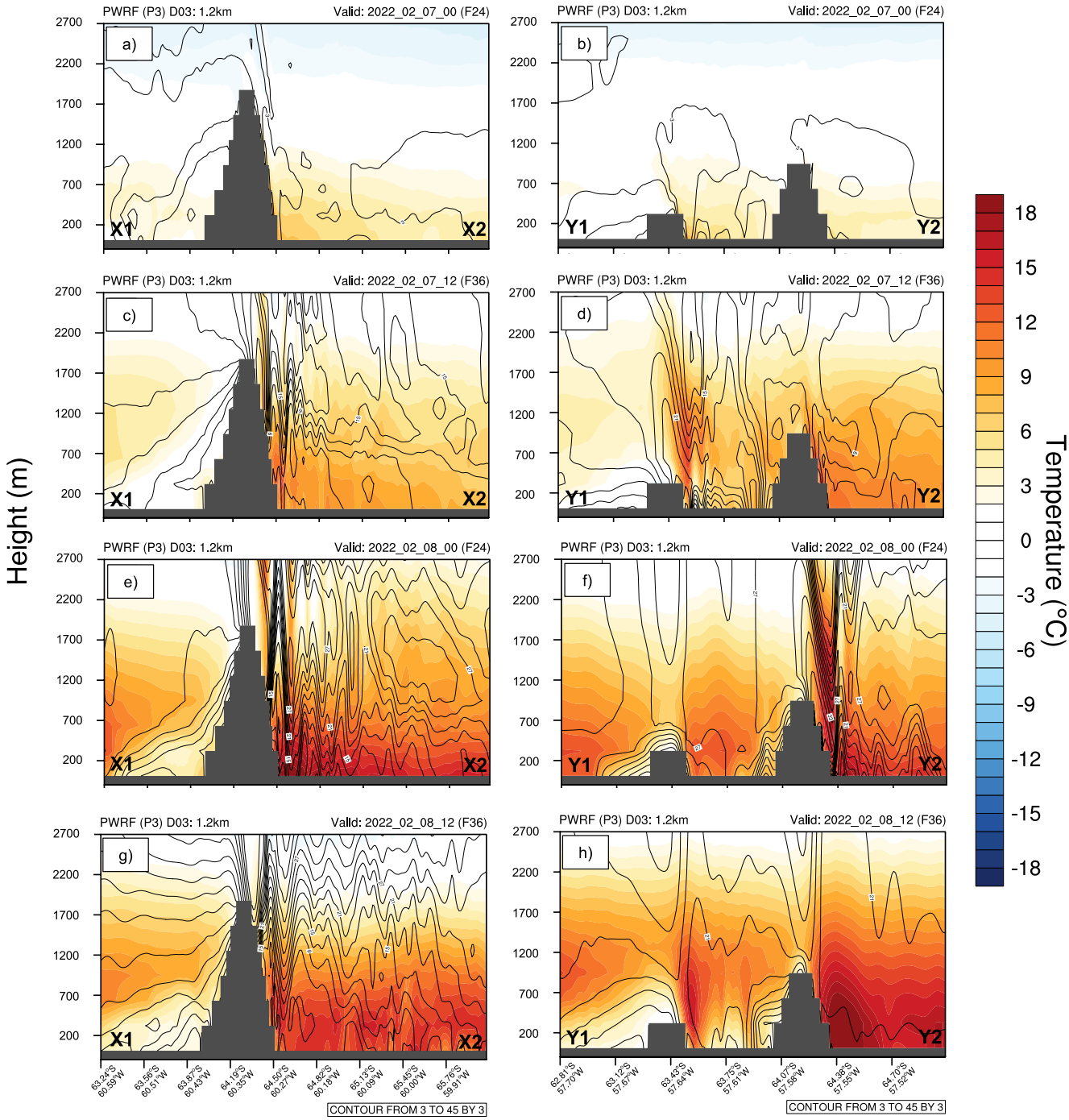

Figure 6. Vertical profiles of horizontal wind speed (u and v, black lines) and physical temperature (filled contours) along two cross-sections across the Antarctic Peninsula. The first, labeled X1-X2 (left panels), crosses Graham land; while the second, Y1-Y2 (right panels) cross Trinity Peninsula (both are indicated in Figure 5b). Cross sections are shown on 7 February 2022 at (a and b) 0000 UTC and (c and d) 1200 UTC, and 8 February (e and f) at 0000 UTC and (g and h) 1200 UTC.

elevation regions (e.g., foehn jets) and potential cloud formation accordingly (Figures S8 and S11 in Supporting Information S1).

Consistent with Laffin et al. (2022), two foehn jets were found over Larsen A and B in high-resolution PWRF outputs during the 2022 event (LA jet and LB jet, Figure 10a). With faster wind speed, lower temperature, and higher relative humidity during the foehn jets (purple boxes in Figures 10b–10d) compared to the background air,

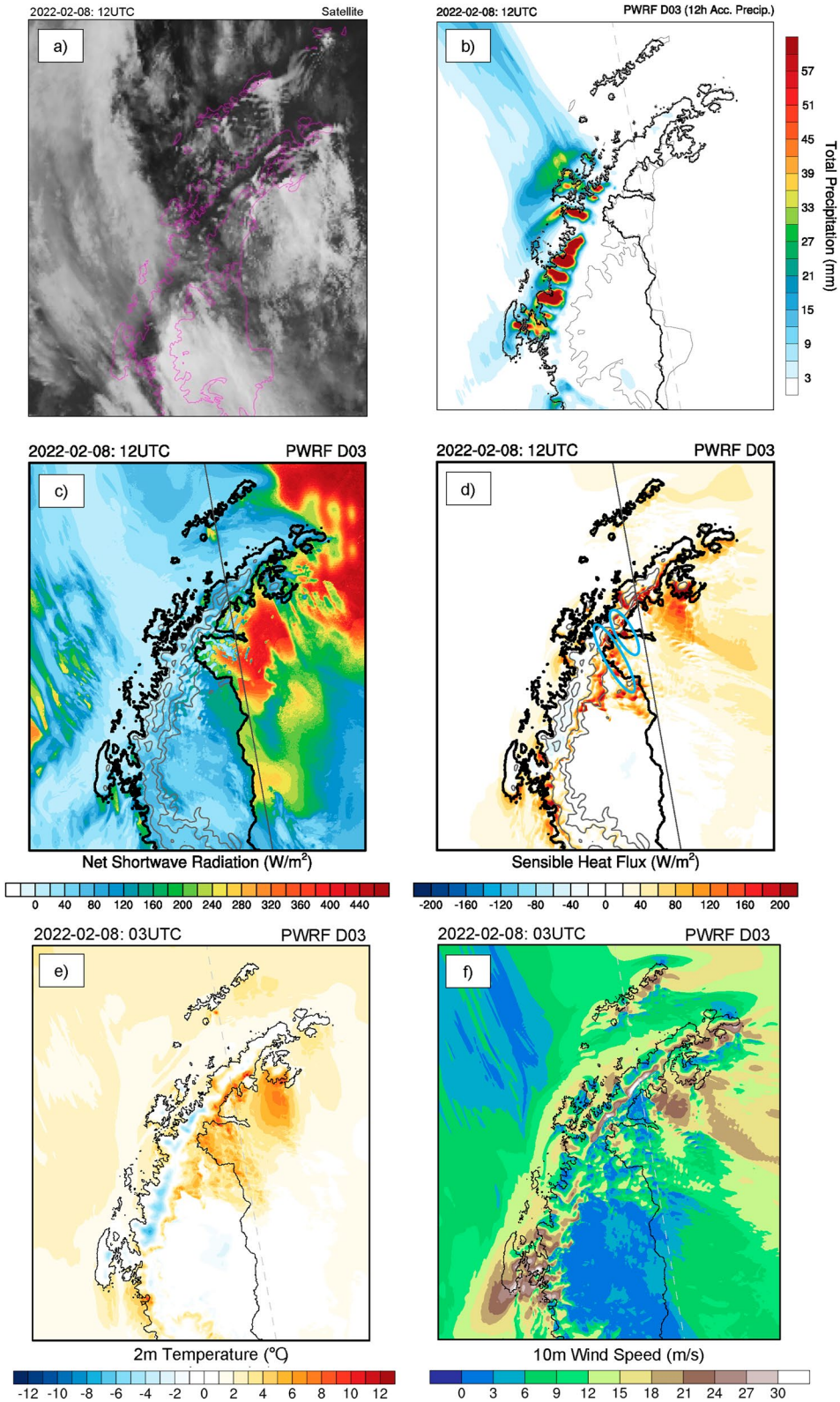

Figure 7. Clouds, precipitation, and the surface energy balance over the Antarctic Peninsula during the daytime, at 1200UTC 8 February 2022. (a) Cloud cover from Antarctic composite infrared data (purple lines indicate the coastline), along with Polar WRF simulations of (b) 12-hr accumulated precipitation (c) Net shortwave radiation, and (d) Sensible heat flux, (e) 2 m temperature, and (f) 10 m horizontal wind speed. Gray lines in (c and d) are meridians.

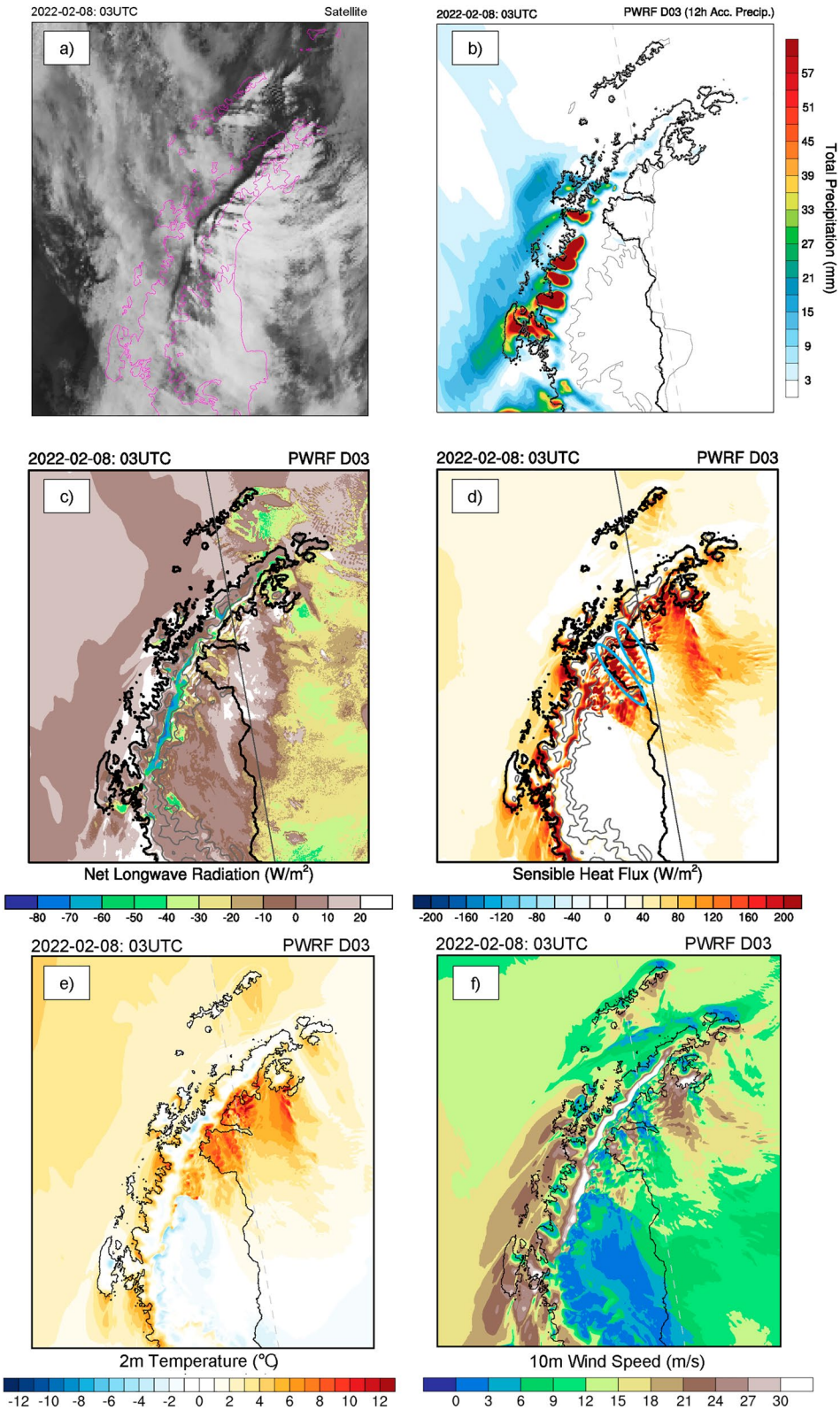

Figure 8. Clouds, precipitation, and the surface energy balance over the Antarctic Peninsula during the nighttime, at 1500 UTC 8 February 2022. (a) Cloud cover from Antarctic composite infrared data (purple lines indicate the coastline), along with Polar WRF simulations of (b) 12-hr accumulated precipitation (c) Net longwave radiation, (d) Sensible heat flux, (e) 2 m temperature, and (f) 10 m horizontal wind speed. Gray lines in (c and d) are meridians.

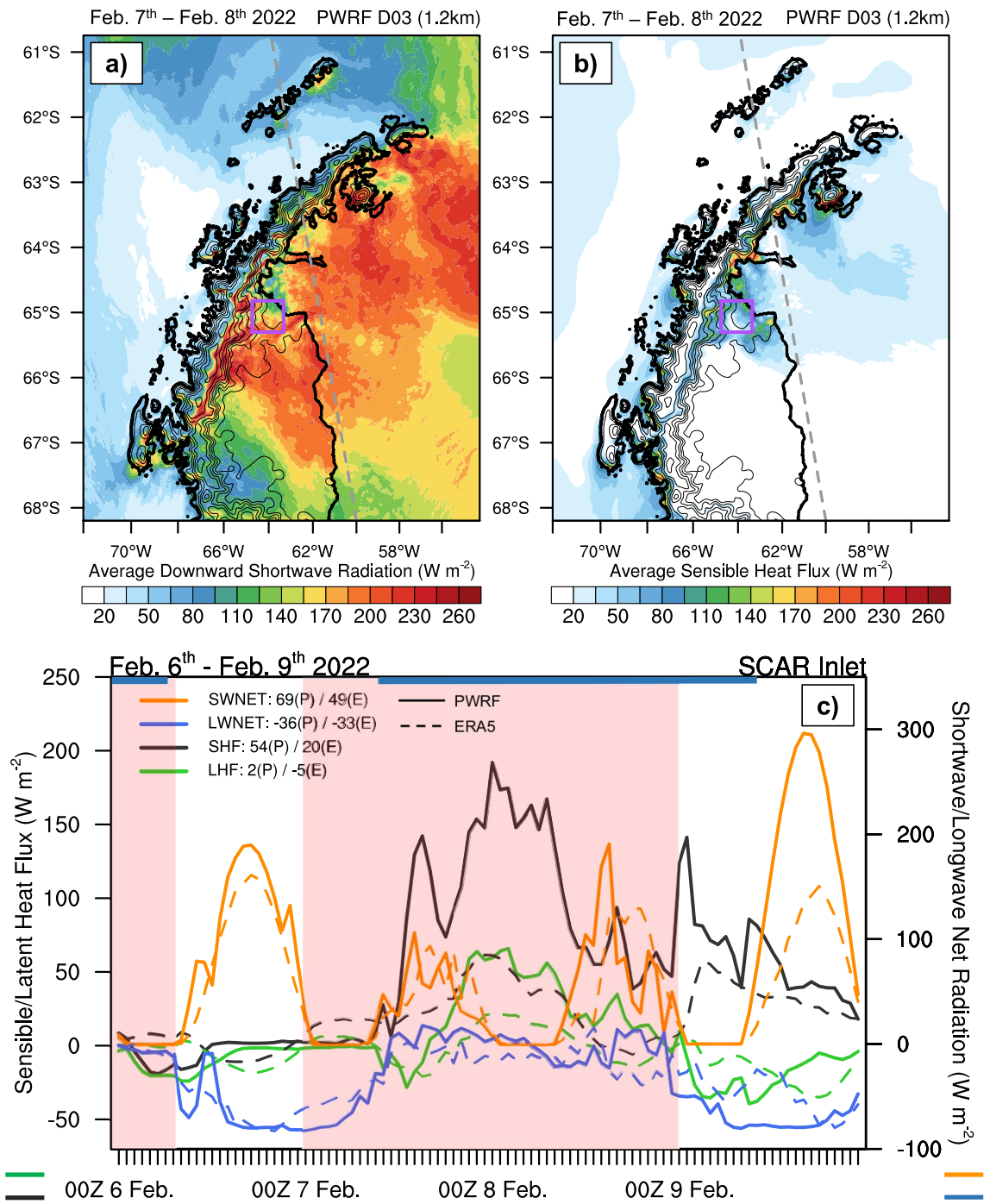

Figure 9. Surface energy balance during the peak of the 2022 6–9 February foehn event over SCAR Inlet, on the Antarctic Peninsula. (a and b) Average downward shortwave radiation and average sensible heat from hourly PWRF simulations. (c) time series of sensible/latent heat flux (refers to left scale) and net shortwave/longwave radiation (refers to right scale) from PWRF simulations (solid lines) and ERA5 reanalysis data (dashed lines) within the purple box shown in (a and b). In (c), the pink shadow indicates the foehn period, while the broken navy line at the top of the panel indicates periods during which an atmospheric river affected the SCAR Inlet. ERA5 reanalysis data is re-gridded to PWRF D03 to provide comparable results.

the two jets created a cooling gap between the two warming spots mentioned before (Figure 5). The maximum wind speed of the jets occurs at ~700 m above the surface (Figure 10b). Because the direction of the marine air advection varies with time, the locations of the jets shift slightly. For instance, the LB jet can affect either the

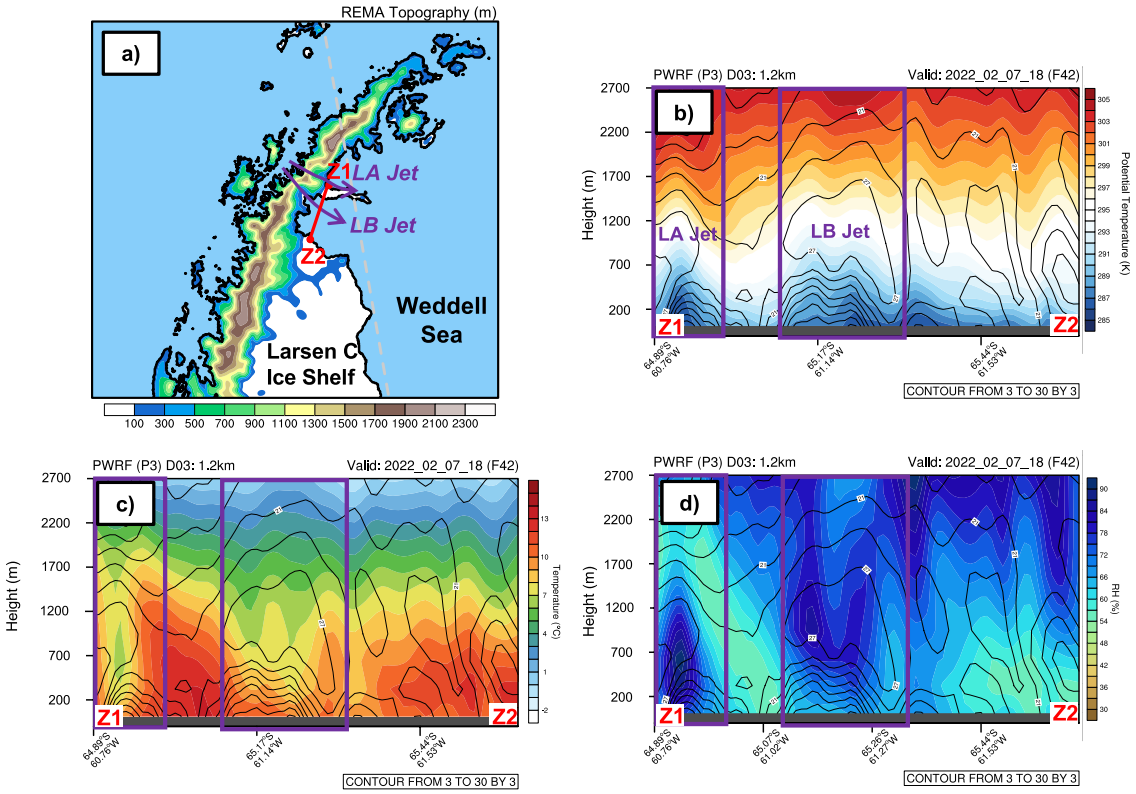

Figure 10. (a) Map of the Antarctic Peninsula showing the Larsen A jet (LA jet) and the Larsen B jet (LB jet) during the February 2022 foehn case. (b–d) Potential temperature, temperature, and relative humidity (RH) with height at 1800 UTC 07 February 2022 (colors), for a cross section perpendicular to the Larsen A and B jets (indicated by the red line from Z1 to Z2 in a). The wind speed is shown by black contour lines.

Larsen B or SCAR Inlet depending on the incoming flow. When the near-surface air is relatively warm, the strong vertical potential temperature gradient can enhance the transfer of sensible heat flux from upper-level air to the surface (e.g., LA jet; Figure 10 and Figure S12 in Supporting Information S1). While SW_{net} (due to the potential cloud formation) may be lower within foehn jets, the strong accompanying winds could accelerate the ice shelf disintegration via pushing ice to the ocean and enhancing SHF (Elvidge et al., 2015; Laffin et al., 2022). However, unlike Elvidge et al. (2015)'s foehn jet study over the Larsen C Ice shelf, where the surface was relatively smooth ice, both the LA and LB jets in 2022 blow over a surface that is a mixture of open water and floating ice (Figure S8in Supporting Information S1). Further research, such as trajectory analysis, is necessary to distinguish all the mechanisms that lead to surface warming.

4. Discussion

The maximum impact of foehn warming is expected to occur when the incoming wind approaches the topographic barrier perpendicularly (e.g., during a zonal wind). Most of the AP region, especially the southern area, will have a stronger foehn warming under the zonal wind (Bozkurt et al., 2018). However, when there is a low over the Bellingshausen Sea and a nearby blocking high over the Weddell Sea, the AP is more likely to experience meridional warm air advection. Given that the northern tip of the AP tilts eastward, it will experience a stronger foehn under a meridional (northerly) wind (Figure S4 in Supporting Information S1). In other words, the northern AP is more vulnerable to the combined impact from foehn and AR under a persistent meridional wind, such as the 2022 case instead of the 2018 case. Also, the vertical structure of the atmosphere on the upwind side also affects the foehn warming. A more stratified atmosphere with slow wind speed will result in a shallow foehn condition, which has low-level blocking on the upwind side and possible hydraulic jumps on the leeside (Durran, 1990). For example, the topographic blocking for the northerly meridional wind at 850 hPa persisted for 11 months during 2002–03 (Orr et al., 2004). In contrast, strong vertical wind shear and unstable atmosphere usually lead to intense orographic lifting on the upwind side and stationary orographic gravity wave on the leeside (Elvidge et al., 2015).

For the 2022 case, the strong AR brings faster and warmer moist air from the lower latitudes over the relatively colder ocean and propagates to the northern AP perpendicularly. On the upwind side, a temperature inversion is observed, as well as strong vertical wind shear due to the low-level jet (~700 m above the surface; not shown). Thus, the 2022 case was characterized by weak low-level blocking and strong mountain waves on the leeside, which made this case closer to a deep foehn scenario. PWRF simulations show a weak-to-moderate hydraulic jump near the mountain peak and stationary mountain waves covering most of the leeside (e.g., Figure 6g). By contrast, the 2015 case study conducted by Bozkurt et al. (2018) has strong low-level blocking on the upwind side (shallow foehn). Instead of the stationary orographic gravity wave, the leeside has a sharp and large hydraulic jump, which leads to the formation of "foehn gaps" (cloud-free zone) along the mountain base. Although shallow foehn often leads to a larger positive temperature anomaly via adiabatic warming (isentropic drawdown) and intensive SHF at the mountain base, deep foehn is more likely to result in extensive surface warming/melting via SHF from stationary orographic waves (Elvidge et al., 2015). The direction and magnitude of AR can complicate the foehn warming via contributing extra moisture and also affect the vertical structure of the atmosphere on the upwind side, which is related to the development of mountain waves on the leeside. This will impact the SHF and cloud conditions, and the surface warming consequently.

Similar to the AP region, the eastern Ross Ice Shelf over WA experienced the combined impact of AR and foehn in a few historic surface melting events. With a blocking high (over the Bellingshausen/Amundsen Sea) and a nearby low-pressure system (over the Amundsen/Ross Sea), coastal WA is more likely to have strong warm marine air advection or ARs (Scott et al., 2019; Zou et al., 2021a). WA can experience extensive LWD from warm and moist air intrusion (Hu et al., 2019), and the eastern RIS on the leeside can have foehn warming subsequently. The local topography over the AP is different from WA. Instead of two relatively gentle mountain ranges (over Marie Byrd Land and Edward VII Land), the AP has one sharp topographic barrier along Graham Land. Thus, the AP usually has stronger foehn warming. In addition, both the AP and eastern RIS can experience foehn clearance and have direct moisture input that potentially led to cloud formation simultaneously. For example, during a 2015 melt event (Ghiz et al., 2021), Siple Dome had a descending warm and dry air mass that might have reduced the optical thickness of the clouds and enhanced all-wave radiation. In the 2022 case, cloud formation on the leeside triggered by the extra moisture via AR and gap flows hampers the SWD at the mountain base but increases the LWD slightly. Although the LA and LB jets reduce temperatures and the impacts from SW_{net}, they could accelerate the ice shelf disintegration via pushing ice to the ocean. The occurrence of AR and complicated local topography introduce more uncertainties to foehn studies over the AP.

The detailed mechanisms of foehn for both regions need to be analyzed case by case. With a colder background temperature, the RIS is at a lower risk of collapsing or intense surface melting. The RIS might experience moderate surface melting during a foehn event in austral summer, and no melt ponding has been reported over the Siple Coast region (Ghiz et al., 2021; Zou et al., 2021b). In contrast, foehn/AR events contributed to the collapse of Larsen A Ice shelf in 1995 and Larsen B Ice Shelf in 2002 (Wille et al., 2022). An increasing AR frequency over the AP may occur in the future under climate change, as well as the positive SAM trend (Espinoza et al., 2018; Wille et al., 2021). Consequently, more intense and complicated foehn cases may occur, which can lead to extreme weather, such as record-breaking temperature and intense precipitation (e.g., Bozkurt et al., 2018; González-Herrero et al., 2022; Gorodetskaya et al., 2023). In addition, the upper Southern Ocean has warmed due to anthropogenic activities since the 1950s, and drastic reductions of ice-shelf extent and surface height over the AP are associated with the basal melting (Armour et al., 2016; Cook & Vaughan, 2010; Li et al., 2021; Paolo et al., 2015). The warm ocean water beneath the ice shelf can sculpt the basal channel, deepen the crevasses, and ultimately penetrate the ice (Watkins et al., 2021). The ice shelf thinning rate on the eastern side of the AP is around half that compared to the western side. However, the south edge of the Larsen C Ice Shelf (Bawden Ice Rise) experiences rapid basal melting, as well as surface melting resulting from AR intrusion and foehn (Adusumilli et al., 2018; Bozkurt et al., 2018). Previous research suggests that the wind forcing associated with ARs and foehn can favor the formation of polynya and oceanic heat transfer (Francis et al., 2019; Pritchard et al., 2012; Reoccurrence of the Maud Rise Polynya in Austral Winter, 2017). Although there is no direct relationship between AR activity and basal melting, the combined surface and ocean warming can accelerate ice shelf break-up (Wille et al., 2022). Future research is also needed to investigate the impact of AR intrusion on ocean currents, which can discharge the coastal ice and transport heat to the ice shelf cavity (Turner et al., 2022).

The fast-changing surface due to the melting and ice loss challenges the ability of numerical weather models to accurately describe surface condition, such as temperature. A more advanced land surface model that can

accurately represent the changing surface dynamically (e.g., albedo and land/sea mask) should be included in PWRF, especially for simulations over the AP region (e.g., Figure S1 in Supporting Information S1). Field observations of cloud properties are needed to help validate model cloud microphysics, as well as its impact on surface warming. Also, a coupled ocean-atmosphere model is needed to provide a more accurate estimation of ice shelf stabilities over the AP region.

5. Summary

The AP region experienced a combined impact from AR and foehn warming during both 2018 and 2022 cases. With a blocking high located at the Weddell Sea during the 2022 case, the northern tip of the AP is hit by a northwesterly AR perpendicularly for 3 days. Thus, compared to the 2018 case, the 2022 case was characterized by stronger and longer lasting foehn warming. Over the Larsen B embayment during the 2022 foehn case, there was an average 2 m temperature increase of 5°C within 24 hr. A low-pressure center to the west of the AP with a blocking high to the east often leads to a stationary circulation pattern, which contributes to poleward moisture transport (Wang, Ding, et al., 2022). The importance of the blocking high to the regional circulation over the AP as well as the rest of the Antarctic continent has been highlighted in multiple research papers. It not only enhances the pressure gradient and accelerates the marine air advection (AR related), but the blocking high also creates a more persistent pattern that results in a longer-lasting event, especially for the northern AP (e.g., Hirasawa et al., 2013; Nicolas et al., 2017; Xu et al., 2021).

The persistent impact of the AR can lead to strong foehn warming along the leeside of the AP, especially from the latent heat release on the upwind side (Bozkurt et al., 2018; Wille et al., 2022). Both 2018 (ENSO-neutral) and 2022 (La Niña) cases have intense precipitation on the western AP, and warm downslope wind on the eastern side. As a deep-foehn like case, the 2022 event has strong stationary orographic gravity waves on the leeside, which enhances heat transfer between the upper foehn flow and the surface (Figure 6). The 2022 case has two warming spots, one over the Larsen B embayment and the other on the leeside of James Ross Island (Figure 5). Between these two spots, there is a relatively cooler gap close to Robertson Island, which is indicative of a strong foehn jet (the LB jet).

During the austral summer, the AP region experiences a strong diurnal cycle. Thus, the lead driver of surface warming is different between daytime and nighttime (Figures 7 and 8). During the daytime, SW_{net} significantly contributes to the surface warming/melting over the SCAR Inlet, followed by the SHF. During the nighttime, SHF is the major driver. Shortwave radiation is associated with foehn clearance, which can be amplified by the AR intrusion. However, in the 2022 case, gap flows/foehn jets significantly contribute to moisture transports on the leeside and reduce SW_{net}, especially at the mountain base. On the other hand, SHF continuously contributes to surface warming, which is highly correlated with the magnitude of the foehn. Overall, SW_{net} is the major contributor to surface warming/melting over the ice surface during the 2022 foehn period, except for the mountain base where SHF has an equal contribution or areas with cloud formation due to the gap flows/foehn jets.

In general, the AR intrusion complicates the foehn warming over the AP region, and usually amplifies the surface warming/melting. First, ARs with longer duration usually propagate toward the AP in a meridional direction, which moves perpendicular to the northern tip but not to the southern AP. Thus, the Larsen C ice shelf will have less foehn warming, but Larsen A and B (including SCAR Inlet) will be under greater impact. Second, there are several gaps along the topographic barrier over the AP, especially over the northern tip. Foehn jets via the low-elevation gap can compensate for the increased SWD resulting from foehn clearance and enhance the SHF. Third, for the 2022 case, SWD is the leading driver for the surface warming over the ice surface with SHF playing a significant role. However, the mechanisms of AR/foehn warming events over the AP vary case by case. ARs can amplify the leeside foehn warming via increased latent heat release on the upwind but can also hamper the foehn clearance via potential cloud formation. Depending on the phase, height, and thickness of clouds on the leeside, the net radiation can vary. All cases need to be analyzed independently and trajectory analysis will help distinguish the impact of each driver. The in-depth analysis of these two cases in this study provides a valuable framework for developing criteria for the long-term analysis of the combined AR and foehn influence on the AP. To better address different types of ARs and their consequent impact, a series of AR events with or without strong foehn warming will be studied during different seasons. Our future research will (a) continue to improve the high-resolution simulations over the AP region; (b) improve our understanding of the relationship of AR and foehn under different synoptic circulation patterns via analyzing more AR/foehns cases; and (c) quantify the

contribution of each driver to surface warming in order to build a better understanding of surface melting over the AP under the influence of climate change.

Data Availability Statement

ERA5 and ERA5 Land reanalysis data are available at Copernicus Climate Change Service (C3S) Climate Date Store. Surface station observations and Antarctic composite infrared satellite imagery data are available at Antarctic Meteorological Research and Data Center (AMRDC) (https://amrdcdata.ssec.wisc.edu/). The Worldview tool from NASA's Earth Observing System Data and Information System (EOSDIS) provides additional satellite imagery (https://worldview.earthdata.nasa.gov/). Moderate Resolution Imaging Spectroradiometer (MODIS) albedo is produced by the National Aeronautics and Space Administration (NASA; https://lpdaac.usgs.gov/products/mcd43c3v006/). Reference Elevation Model of Antarctica (REMA) topography used in PWRF is available at https://www.envidat.ch/dataset/rema-topography-and-antarcticalc2000-for-wrf. PWRF model is available upon request at Polar Meteorology Group, Byrd Polar and Climate Research Center, The Ohio State University. Figures were made with the NCAR Command Language (Version 6.6.2).

Acknowledgments

This collaborative research was supported by National Science Foundation (NSF) Grants 2127632, 2229392 and FIRO2 W912HZ-19-2-0023 (U.S. Army Corps of Engineers). I.V.G. thanks the support by the strategic funding to CESAM (Grant UIDP/50017/2020, UIDB/50017/2020, and LA/P/0094/2020), to CIIMAR (UIDB/04423/2020, UIDP/04423/2020), 2021.03140. CEECIND and Project ATLACE (CIRCNA/CAC/0273/2019) through national funds provided by FCT–Fundação para a Ciência e a Tecnologia. D.H.B. acknowledges support from NSF Grant 2205398. M.A.L. acknowledges support from NSF Grants 1924730, 1951603, 1951720. J.D.W. acknowledges support from the Agence Nationale de la Recherche projects ANR-20-CE01-0013 (ARCA). R.R.C. thanks the support of INACH (Preis RT_69-20) and ANID (Preis FONDECYT 1191932 and ANILLO ACT210046). The Polar WRF model is developed and is maintained by the Polar Meteorology Group, Byrd Polar and Climate Research Center (BPCRC), The Ohio State University. Contribution number 1607 of BPCRC. Polar WRF simulations were performed on the San Diego Supercomputing Center's COMET resource through AR Program, Phase II 460001361 and III 4600014294 (State of California, Department of Water Resources). We are grateful to the Instituto Antarctica Argentino (IAA/DNA), the Servicio Meteorologico Nacional (SMN), the Integrated Global Radiosonde Archive for radiosonde and surface meteorological data from Marambio Station, the Dirección Meteorológica de Chile (DMC), and to the Instituto Antartico Chileno (INACH) for supporting observations in the Antarctic Peninsula. We acknowledge the use of imagery from the NASA Worldview application (https://worldview.earthdata.nasa.gov/), part of the NASA Earth Observing System Data and Information System (EOSDIS). We also want to thank Diego Campos and Edgardo Sepulveda for radiosonde measurements and Dr. Matthew Mazloff for his input on the role of oceanic processes during the AR intrusion. We thank the three anonymous reviewers for their many constructive suggestions.

References

Adusumilli, S., Fricker, H. A., Siegfried, M. R., Padman, L., Paolo, F. S., & Ligtenberg, S. R. M. (2018). Variable basal melt rates of Antarctic Peninsula ice shelves, 1994–2016. *Geophysical Research Letters*, *45*(9), 4086–4095. https://doi.org/10.1002/2017GL076652

Armour, K. C., Marshall, J., Scott, J. R., Donohoe, A., & Newsom, E. R. (2016). Southern Ocean warming delayed by circumpolar upwelling and equatorward transport. *Nature Geoscience*, *9*(7), 549–554. https://doi.org/10.1038/ngeo2731

Antarctic Meteorological Research and Data Center. (2021). Antarctic satellite composite imagery animations Dataset. AMRDC Data Repository. https://doi.org/10.48567/hevb-j127

Bodas-Salcedo, A., Hill, P. G., Furtado, K., Williams, K. D., Field, P. R., Manners, J. C., et al. (2016). Large contribution of supercooled liquid clouds to the solar radiation budget of the Southern Ocean. *Journal of Climate*, *29*(11), 4213–4228. https://doi.org/10.1175/JCLI-D-15-0564.1

Bozkurt, D., King, D., Kennett, J. C., & Turner, J. (2022). Central tropical Pacific convection drives extreme high temperatures and surface melt on the Larsen C Ice Shelf, Antarctic Peninsula. *Nature Communications*, *13*(1), 3906. https://doi.org/10.1038/s41467-022-31119-4

Bozkurt, D., Rondanelli, R., Marín, J. C., & Garreaud, R. (2018). Foehn event triggered by an Atmospheric River underlies record-setting temperature along continental Antarctica. *Journal of Geophysical Research: Atmospheres*, *123*(8), 3871–3892. https://doi.org/10.1002/2017JD027796

Bromwich, D. H., Otieno, F. O., Hines, K. M., Manning, K. W., & Shilo, E. (2013). Comprehensive evaluation of polar weather research and forecasting model performance in the Antarctic. *Journal of Geophysical Research: Atmospheres*, *118*(2), 274–292. https://doi.org/10.1029/2012JD018139

Bromwich, D. H., Werner, K., Casati, B., Powers, J. G., Gorodetskaya, I. V., Massonnet, F., et al. (2020). The year of polar prediction in the southern hemisphere (YOPP-SH). *Bulletin of the American Meteorological Society*, *101*(10), E1653–E1676. https://doi.org/10.1175/BAMS-D-19-0255.1

Chyhareva, A., Gorodetskaya, I., Krakovska, S., Pishniak, D., & Rowe, P. (2021). Precipitation phase transition in austral summer over the Antarctic Peninsula. *Ukrainian Antarctic journal*, (1), 32–46. https://doi.org/10.33275/1727-7485.1.2021.664

Clem, K. R., Renwick, J. A., McGregor, J., & Fogt, R. L. (2016). The relative influence of ENSO and SAM on Antarctic Peninsula climate. *Journal of Geophysical Research: Atmospheres*, *121*(16), 9324–9341. https://doi.org/10.1002/2016JD025305

Clough, S. A., Shephard, M. W., Mlawer, E. J., Delamere, J. S., Iacono, M. J., Cady-Pereira, K., et al. (2005). Atmospheric radiative transfer modeling: A summary of the AER codes. *Journal of Quantitative Spectroscopy and Radiative Transfer*, *91*(2), 233–244. https://doi.org/10.1016/j.jqsrt.2004.05.058

Cook, A. J., & Vaughan, D. G. (2010). Overview of areal changes of the ice shelves on the Antarctic Peninsula over the past 50 years. *The Cryosphere*, *4*(1), 77–98. https://doi.org/10.5194/tc-4-77-2010

Corbea-Pérez, A., Calleja, J. F., Recondo, C., & Fernández, S. (2021). Evaluation of the MODIS (C6) daily albedo products for Livingston Island, Antarctic. *Remote Sensing*, *13*(12), 2357. https://doi.org/10.3390/rs13122357

Davis, S. M., Hegglin, M. I., Fujiwara, M., Dragani, R., Harada, Y., Kobayashi, C., et al. (2017). Assessment of upper tropospheric and stratospheric water vapor and ozone in reanalyses as part of S-RIP. *Atmospheric Chemistry and Physics*, *17*(20), 12743–12778. https://doi.org/10.5194/acp-17-12743-2017

Durran, D. R. (1990). (Eds.). Mountain waves and downslope winds. *Atmospheric Processes over complex terrain*. In *Meteorological monographs* (pp. 59–81). American Meteorological Society.

Eayrs, C., Li, X., Raphael, M. N., & Holland, D. M. (2021). Rapid decline in Antarctic sea ice in recent years hints at future change. *Nature Geoscience*, *14*(7), 460–464. https://doi.org/10.1038/s41561-021-00768-3

Elvidge, A. D., & Renfrew, I. A. (2016). The causes of Foehn warming in the lee of mountains. *Bull. Amer. Meteor.*, *97*(3), 455–466. https://doi.org/10.1175/BAMS-D-14-00194.1

Elvidge, J. C., King, A., Orr, T. A., Lachlan-Cope, M. W., & Gray, S. L. (2015). Foehn jets over the Larsen C Ice Shelf, Antarctica. *Quarterly Journal of the Royal Meteorological Society*, *141*(688), 698–713. https://doi.org/10.1002/qj.2382

ElvidgeMunneke, P. K., King, J. C., Renfrew, I. A., & Gilbert, E. (2020). Atmospheric drivers of melt on Larsen C Ice Shelf: Surface energy budget regimes and the impact of foehn. *Journal of Geophysical Research: Atmospheres*, *125*, e2020JD032463. https://doi.org/10.1029/2020JD032463

Espinoza, V., Waliser, D. E., Guan, B., Lavers, D. A., & Ralph, F. M. (2018). Global analysis of climate change projection effects on atmospheric rivers. *Geophysical Research Letters*, *45*(9), 4299–4308. https://doi.org/10.1029/2017GL076968

Feron, S., Cordero, R. R., Damiani, A., Malhotra, A., Seckmeyer, G., & Llanillo, P. (2021). Warming events projected to become more frequent and last longer across Antarctica. *Scientific Reports*, *11*(1), 19564. https://doi.org/10.1038/s41598-021-98619-z

Gerber, F., & Lehning, M. (2020). REMA topography and AntarcticaLC2000 for WRF. *EnviDat*. https://doi.org/10.16904/envidat.190

Ghiz, M. L., Scott, R. C., Vogelmann, A. M., Lenaerts, J. T. M., Lazzara, M., & Lubin, D. (2021). Energetics of surface melt in West Antarctica. *The Cryosphere*, *15*(7), 3459–3494. https://doi.org/10.5194/tc-15-3459-2021

González-Herrero, S., Barriopedro, D., Trigo, R. M., López-Bustins, J. A., & Oliva, M. (2022). Climate warming amplified the 2020 record-breaking heatwave in the Antarctic Peninsula. *Communications Earth & Environment*, *3*(1), 122. https://doi.org/10.1038/s43247-022-00450-5

Gorodetskaya, I. V., Durán-Alarcón, C., Gonzalez-Herrero, S., Clem, K., Rodriguez Imazio, P., Leroy-Dos Santos, C., et al. (2023). Compound drivers behind new record high temperatures and surface melt at the Antarctic Peninsula in February 2022. 01 March 2023, PREPRINT. *Under review, NPJ Clim. Atmos. Sci*. (Version 1). https://doi.org/10.21203/rs.3.rs-2544063/v1

Gorodetskaya, I. V., Silva, T., Schmithüsen, H., & Hirasawa, N. (2020). Atmospheric River signatures in radiosonde profiles and reanalyses at the Dronning Maud Land Coast, East Antarctica. *Advances in Atmospheric Sciences*, *37*(5), 455–476. https://doi.org/10.1007/s00376-020-9221-8

Hersbach, H., Bell, B., Berrisford, P., Biavati, G., Horányi, A., Muñoz Sabater, J., et al. (2018). ERA5 hourly data on single levels from 1940 to present Dataset. Copernicus Climate Change Service (C3S) Climate Data Store (CDS). https://doi.org/10.24381/cds.adbb2d47

Hersbach, H., Bell, B., Berrisford, P., Hirahara, S., Horanyi, A., Muñoz-Sabater, J., et al. (2020). The ERA5 global reanalysis. *Quarterly Journal of the Royal Meteorological Society*, *146*(730), 1999–2049. https://doi.org/10.1002/qj.3803

Hines, K. M., & Bromwich, D. H. (2008). Development and testing of polar weather research and forecasting (WRF) model. Part I: Greenland ice sheet meteorology. *Monthly Weather Review*, *136*(6), 1971–1989. https://doi.org/10.1175/2007MWR2112.1

Hines, K. M., Bromwich, D. H., Silber, I., Russell, L. M., & Bai, L. (2021). Predicting frigid mixed-phase clouds for pristine coastal Antarctica. *Journal of Geophysical Research: Atmospheres*, *126*, e2021JD035112. https://doi.org/10.1029/2021JD035112

Hines, S.-H., Wang, I. S., Verlinde, J., & Lubin, D. (2019). Microphysics of summer clouds in central West Antarctica simulated by the polar weather research and forecasting model (WRF) and the Antarctic Mesoscale Prediction System (AMPS). *Atmospheric Chemistry and Physics*, *19*, 12431–12454. https://doi.org/10.5194/acp-19-12431-2019

Hirasawa, N., Nakamura, H., Motoyama, H., Hayashi, M., & Yamanouchi, T. (2013). The role of synoptic-scale features and advection in prolonged warming and generation of different forms of precipitation at Dome Fuji station, Antarctica, following a prominent blocking event. *Journal of Geophysical Research: Atmospheres*, *118*(13), 6916–6928. https://doi.org/10.1002/jgrd.50532

Hoffmann, L., Günther, G., Li, D., Stein, O., Wu, X., Griessbach, S., et al. (2019). From ERA-interim to ERA5: The considerable impact of ECMWF's next-generation reanalysis on Lagrangian transport simulations. *Atmospheric Chemistry and Physics*, *19*(5), 3097–3124. https://doi.org/10.5194/acp-19-3097-2019

Holland, P. R., Corr, H. F. J., Pritchard, H. D., Vaughan, D. G., Arthern, R. J., Jenkins, A., & Tedesco, M. (2011). The air content of Larsen Ice Shelf. *Geophysical Research Letters*, *38*(10). https://doi.org/10.1029/2011GL047245

Howat, I. M., Porter, C., Smith, B. E., Noh, M.-J., & Morin, P. (2019). The reference elevation model of Antarctica. *The Cryosphere*, *13*(2), 665–674. https://doi.org/10.5194/tc-13-665-2019

Hu, X., Sejas, S. A., Cai, M., Li, Z., & Yang, S. (2019). Atmospheric dynamics footprint on the January 2016 ice sheet melting in West Antarctica. *Geophysical Research Letters*, *46*(5), 2829–2835. https://doi.org/10.1029/2018GL081374

Jakobs, C. L., Reijmer, C. H., van den Broeke, M. R., van de Berg, W. J., & van Wessem, J. M. (2021). Spatial variability of the snowmelt-albedo feedback in Antarctica. *Journal Geophysical Research: Earth Surface*, *126*(2), e2020JF005696. https://doi.org/10.1029/2020JF005696

Jones, M. E., Bromwich, D. H., Nicolas, J. P., Carrasco, J., Plavcová, E., Zou, X., & Wang, S.-H. (2019). Sixty years of widespread warming in the southern middle and high latitudes (1957–2016). *Journal of Climate*, *32*(20), 6875–6898. https://doi.org/10.1175/JCLI-D-18-0565.1

Kain, J. S. (2004). The Kain–Fritsch convective parameterization: An update. *Journal of Applied Meteorology and Climatology*, *43*(1), 170–181. https://doi.org/10.1175/1520-0450(2004)043<0170:TKCPAU>2.0.CO;2

Kuipers Munneke, P., Luckman, A. J., Bevan, S. L., Smeets, C. J. P. P., Gilbert, E., van den Broeke, M. R., et al. (2018). Intense winter surface melt on an Antarctic ice shelf. *Geophysical Research Letters*, *45*(15), 7615–7623. https://doi.org/10.1029/2018GL077899

Laffin, M. K., Zender, C. S., Singh, S., Van Wessem, J. M., Smeets, C. J. P. P., & Reijmer, C. H. (2021). Climatology and evolution of the Antarctic Peninsula Föhn wind-induced melt regime From 1979–2018. *Journal of Geophysical Research: Atmospheres*, *126*(4), e2020JD033682. https://doi.org/10.1029/2020JD033682

Laffin, M. K., Zender, C. S., van Wessem, M., & Marinsek, S. (2022). The role of föhn winds in eastern Antarctic Peninsula rapid ice shelf collapse. *The Cryosphere*, *16*(4), 1369–1381. https://doi.org/10.5194/tc-16-1369-2022

Lazzara, M. A., Weidner, G. A., Keller, L. M., Thom, J. E., & Cassano, J. J. (2012). Antarctic Automatic Weather Station Program: 30 Years of polar observation. *Bulletin of the American Meteorological Society*, *93*(10), 1519–1537. https://doi.org/10.1175/BAMS-D-11-00015.1

Li, X., Cai, W., Meehl, G. A., Chen, D., Yuan, X., Raphael, M., et al. (2021). Tropical teleconnection impacts on Antarctic climate changes. *Nature Reviews Earth & Environment*, *2*(10), 680–698. https://doi.org/10.1038/s43017-021-00204-5

Listowski, C., Delanoë, J., Kirchgaessner, A., Lachlan-Cope, T., & King, J. (2019). Antarctic clouds, supercooled liquid water and mixed phase, investigated with DARDAR: Geographical and seasonal variations. *Atmospheric Chemistry and Physics*, *19*(10), 6771–6808. https://doi.org/10.5194/acp-19-6771-2019

Listowski, C., & Lachlan-Cope, T. (2017). The microphysics of clouds over the Antarctic Peninsula – Part 2: Modelling aspects within polar WRF. *Atmospheric Chemistry and Physics*, *17*, 10195–10221. https://doi.org/10.5194/acp-17-10195-2017

Luckman, A., Elvidge, A., Jansen, D., Kulessa, B., Munneke, P. K., King, J., & Barrand, N. E. (2014). Surface melt and ponding on Larsen C Ice Shelf and the impact of föhn winds. *Antarctic Science*, *26*(6), 625–635. https://doi.org/10.1017/S0954102014000339

Marshall, A. O., van Lipzig, N. P. M., & King, J. C. (2006). The impact of a changing southern hemisphere annular mode on Antarctic Peninsula summer temperatures. *Journal of Climate*, *19*(20), 5388–5404. https://doi.org/10.1175/JCLI3844.1

Marshall, G. J. (2003). Trends in the southern annular mode from observations and reanalyses. *Journal of Climate*, *16*(24), 4134–4143. https://doi.org/10.1175/1520-0442(2003)016<4134:TITSAM>2.0.CO;2

Mattingly, K. S., Mote, T. L., Fettweis, X., van As, D., Tricht, K. V., Lhermitte, S., et al. (2020). Strong summer atmospheric rivers trigger Greenland ice sheet melt through spatially varying surface energy balance and cloud regimes. *Journal of Climate*, *33*(16), 6809–6832. https://doi.org/10.1175/JCLI-D-19-0835.1

MODIS Corrected Reflectance imagery are used from imagery from the NASA Worldview application. [Dataset]. Retrieved from https://worldview.earthdata.nasa.gov/

Mulvaney, R., Abram, N. J., Hindmarsh, R. C. A., Arrowsmith, C., Fleet, L., Triest, J., et al. (2012). Recent Antarctic Peninsula warming relative to Holocene climate and ice-shelf history. *Nature*, *489*(7414), 141–144. https://doi.org/10.1038/nature11391

Muñoz Sabater, J. (2019). ERA5-Land hourly data from 1950 to present Copernicus climate change Service (C3S) Dataset. Climate Data Store (CDS). https://doi.org/10.24381/cds.e2161bac

Muñoz-Sabater, J., Dutra, E., Agustí-Panareda, A., Albergel, C., Arduini, G., Balsamo, G., et al. (2021). ERA5-Land: A state-of-the-art global reanalysis dataset for land applications. *Earth System Science Data*, *13*(9), 4349–4383. https://doi.org/10.5194/essd-13-4349-2021

Nakanishi, M., & Niino, H. (2006). An improved Mellor–Yamada level-3 model: Its numerical stability and application to a regional prediction of advection fog. *Boundary-Layer Meteorology*, *119*(2), 397–407. https://doi.org/10.1007/s10546-005-9030-8

Nicolas, J. P., Vogelmann, A. M., Scott, R. C., Wilson, A. B., Cadeddu, M. P., Bromwich, D. H., et al. (2017). January 2016 extensive summer melt in West Antarctica favoured by strong El Niño. *Nature Communications*, *8*(1), 15799. https://doi.org/10.1038/ncomms15799

Niu, G.-Y., Yang, Z. L., Mitchell, K. E., Chen, F., Ek, M. B., Kumar, A., et al. (2011). The community Noah land surface model with multiparameterization options (Noah-MP): 1. Model description and evaluation with local-scale measurements. *Journal of Geophysical Research*, *116*(D12), D12109. https://doi.org/10.1029/2010JD015139

Orr, A., Cresswell, D., Marshall, G. J., Hunt, J. C. R., Sommeria, J., Wang, C. G., & Light, M. (2004). A 'low-level' explanation for the recent large warming trend over the western Antarctic Peninsula involving blocked winds and changes in zonal circulation. *Geophysical Research Letters*, *31*(6). https://doi.org/10.1029/2003GL019160

Paolo, F. S., Fricker, H. A., & Padman, L. (2015). Volume loss from Antarctic ice shelves is accelerating. *Science*, *348*(6232), 327–331. https://doi.org/10.1126/science.aaa0940

Polar WRF February 2022 Release (Version 4.3.3). [Software]. Retrieved from https://polarmet.osu.edu/PWRF/

Powers, J. G., Manning, K. W., Bromwich, D. H., Cassano, J. J., & Cayette, A. M. (2012). A decade of Antarctic science support through amps. *Bull. Amer. Meteor.*, *93*(11), 1699–1712. https://doi.org/10.1175/BAMS-D-11-00186.1

Pritchard, H. D., Ligtenberg, S. R. M., Fricker, H. A., Vaughan, D. G., van den Broeke, M. R., & Padman, L. (2012). Antarctic ice-sheet loss driven by basal melting of ice shelves. *Nature*, *484*(7395), 502–505. https://doi.org/10.1038/nature10968

Ralph, F. M., Neiman, P. J., & Wick, G. A. (2004). Satellite and CALJET Aircraft observations of atmospheric rivers over the eastern North Pacific Ocean during the Winter of 1997/98. *Monthly Weather Review*, *132*(7), 1721–1745. https://doi.org/10.1175/1520-0493(2004)132<1721:SACAOO>2.0.CO;2

RalphRutz, J. J., Cordeira, J. M., Dettinger, M., Anderson, M., Reynolds, D., Schick, L. J., & Smallcomb, C. (2019). A scale to characterize the strength and impacts of atmospheric rivers. *Bulletin of the American Meteorological Society*, *100*(2), 269–289. https://doi.org/10.1175/BAMS-D-18-0023.1

Reoccurrence of the Maud Rise Polynya in Austral Winter. (2017). *Journal of Geophysical Research: Atmospheres*, *124*, 5251–5267. https://doi.org/10.1029/2019JD030618

Rignot, E., Casassa, G., Gogineni, P., Krabill, W., Rivera, A., & Thomas, R. (2004). Accelerated ice discharge from the Antarctic Peninsula following the collapse of Larsen B ice shelf. *Geophysical Research Letters*, *31*(18), L18401. https://doi.org/10.1029/2004GL020697

Rignot, E., Mouginot, J., Scheuchl, B., van den Broeke, M., van Wessem, M. J., & Morlighem, M. (2019). Four decades of Antarctic ice sheet mass balance from 1979–2017. *Proceedings of the National Academy of Sciences*, *116*(4), 1095–1103. https://doi.org/10.1073/pnas.1812883116

Rott, H., Skvarca, P., & Nagler, T. (1996). Rapid collapse of Northern Larsen Ice Shelf, Antarctica. *Science*, *271*(5250), 788–792. https://doi.org/10.1126/science.271.5250.788

Scambos, T. A., Hulbe, C., Fahnestock, M., & Bohlander, J. (2000). The link between climate warming and break-up of ice shelves in the Antarctic Peninsula. *Journal of Glaciology*, *46*(154), 516–530. https://doi.org/10.3189/172756500781833043

Schaaf, C., & Wang, Z. (2021). MODIS/Terra+Aqua BRDF/albedo albedo daily L3 Dataset. Global 0.05Deg CMG V061. NASA EOSDIS Land Processes DAAC. https://doi.org/10.5067/MODIS/MCD43C3.061

Scott, R. C., Nicolas, J. P., Bromwich, D. H., Norris, J. R., & Lubin, D. (2019). Meteorological drivers and large-scale climate forcing of west Antarctic surface melt. *Journal of Climate*, *32*(3), 665–684. https://doi.org/10.1175/JCLI-D-18-0233.1

Shepherd, A., & Coauthors (2018). Mass balance of the Antarctic ice sheet from 1992 to 2017. *Nature*, *558*(7709), 219–222. https://doi.org/10.1038/s41586-018-0179-y

Siegert, M., Atkinson, A., Banwell, A., Brandon, M., Convey, P., Davies, B., et al. (2019). The Antarctic Peninsula under a 1.5°C global warming scenario. *Frontiers of Environmental Science*, *7*. https://doi.org/10.3389/fenvs.2019.00102

Smith, B., Fricker, H. A., Gardner, A. S., Medley, B., Nilsson, J., Paolo, F. S., et al. (2020). Pervasive ice sheet mass loss reflects competing ocean and atmosphere processes. *Science*, *368*(6496), 1239–1242. https://doi.org/10.1126/science.aaz5845

Terpstra, A., Gorodetskaya, I. V., & Sodemann, H. (2021). Linking sub-tropical evaporation and extreme precipitation over east Antarctica: An Atmospheric River case study. *Journal of Geophysical Research: Atmospheres*, *126*(9), e2020JD033617. https://doi.org/10.1029/2020JD033617

Tetzner, D., Thomas, E., & Allen, C. (2019). A validation of ERA5 reanalysis data in the southern Antarctic Peninsula—Ellsworth land region, and its implications for ice core studies. *Geosciences*, *9*(7), 289. https://doi.org/10.3390/geosciences9070289

The NCAR Command Language. (2019). Release Version 6.6.2 Software. UCAR/NCAR/CISL/TDD. https://doi.org/10.5065/D6WD3XH5

Tuckett, P. A., Ely, J. C., Sole, A. J., Livingstone, S. J., Davison, B. J., van Melchior, Wessem J., & Howard, J. (2019). Rapid accelerations of Antarctic Peninsula outlet glaciers driven by surface melt. *Nature Communications*, *10*(1), 4311. https://doi.org/10.1038/s41467-019-12039-2

Turner, J., Lu, H., King, J. C., Carpentier, S., Lazzara, M., Phillips, T., & Wille, J. (2022). An extreme high temperature event in coastal east Antarctica associated with an Atmospheric River and record summer downslope winds. *Geophysical Research Letters*, *49*(4), e2021GL097108. https://doi.org/10.1029/2021GL097108

Turton, J. V., Kirchgaessner, A., Ross, A. N., & King, J. C. (2018). The spatial distribution and temporal variability of föhn winds over the Larsen C ice shelf, Antarctica. *Quarterly Journal of the Royal Meteorological Society*, *144*(713), 1169–1178. https://doi.org/10.1002/qj.3284

van den Broeke, M. (2005). Strong surface melting preceded collapse of Antarctic Peninsula ice shelf. *Geophysical Research Letters*, *32*(12). https://doi.org/10.1029/2005GL023247

Wang, D., Liang, S., He, T., Yu, Y., Schaaf, C., & Wang, Z. (2015). Estimating daily mean land surface albedo from MODIS data. *Journal of Geophysical Research: Atmospheres*, *120*(10), 4825–4841. https://doi.org/10.1002/2015JD023178

Wang, J., Luo, H., Yang, Q., Liu, J., Yu, L., Shi, Q., & Han, B. (2022). An unprecedented record low Antarctic Sea-ice extent during Austral Summer 2022. *Advances in Atmospheric Sciences*, *39*(10), 1591–1597. https://doi.org/10.1007/s00376-022-2087-1

Wang, S., Ding, M., Liu, G., & Chen, W. (2022). Processes and mechanisms of persistent extreme rainfall events in the Antarctic Peninsula during Austral Summer. *Journal of Climate*, *35*(12), 3643–3657. https://doi.org/10.1175/JCLI-D-21-0834.1

Watkins, R. H., Bassis, J. N., & Thouless, M. D. (2021). Roughness of ice shelves is correlated with basal melt rates. *Geophysical Research Letters*, *48*(21), e2021GL094743. https://doi.org/10.1029/2021GL094743

Wille, J. D., Favier, V., Dufour, A., Gorodetskaya, I. V., Turner, J., Agosta, C., & Codron, F. (2019). West Antarctic surface melt triggered by atmospheric rivers. *Nature Geoscience*, *12*(11), 911–916. https://doi.org/10.1038/s41561-019-0460-1

Wille, J. D., Favier, V., Jourdain, N. C., Kittel, C., Turton, J. V., Agosta, C., et al. (2021). Antarctic Atmospheric River climatology and precipitation impacts. *Journal of Geophysical Research: Atmospheres*, *126*, e2020JD033788. https://doi.org/10.1029/2020JD033788

Wille, J. D., Favier, V., Gorodetskaya, I. V., Agosta, C., Kittel, C., Beeman, J. C., et al. (2022). Intense atmospheric rivers can weaken ice shelf stability at the Antarctic Peninsula. *Communications Earth & Environment*, *3*, 1–14. https://doi.org/10.1038/s43247-022-00422-9

Xu, M., Yu, L., Liang, K., Vihma, T., Bozkurt, D., Hu, X., & Yang, Q. (2021). Dominant role of vertical air flows in the unprecedented warming on the Antarctic Peninsula in February 2020. *Communications Earth & Environment*, *2*, 1–9. https://doi.org/10.1038/s43247-021-00203-w

Xue, J., Xiao, Z., Bromwich, D. H., & Bai, L. (2022). Polar WRF V4.1.1 simulation and evaluation for the Antarctic and Southern Ocean. *Frontiers of Earth Science*, *16*(4), 1005–1024. https://doi.org/10.1007/s11707-022-0971-8

Zou, X., Bromwich, D. H., Montenegro, A., Wang, S.-H., & Bai, L. (2021a). Major surface melting over the Ross Ice Shelf part I: Foehn effect. *Quarterly Journal of the Royal Meteorological Society*, *147*(738), 2874–2894. https://doi.org/10.1002/qj.4104

Zou, X., Bromwich, D. H., Montenegro, A., Wang, S., & Bai, L. (2021b). Major surface melting over the Ross Ice Shelf part II: Surface energy balance. *Quarterly Journal of the Royal Meteorological Society*, *147*(738), 2895–2916. https://doi.org/10.1002/qj.4105

References From the Supporting Information

Loeb, N. G., Doelling, D. R., Wang, H., Su, W., et al. (2018). Clouds and the Earth's radiant energy system (CERES) energy balanced and Filled (EBAF) top-of-atmosphere (TOA) edition-4.0 data product. *Journal of Climate*, *31*(2), 895–918. https://doi.org/10.1175/JCLI-D-17-0208.1